

# CFBDSIR 2149-0403: young isolated planetary-mass object or high-metallicity low-mass brown dwarf?★

P. Delorme<sup>1</sup>, T. Dupuy<sup>2</sup>, J. Gagné<sup>3,★★</sup>, C. Reylé<sup>4</sup>, T. Forveille<sup>1</sup>, M. C. Liu<sup>5</sup>, E. Artigau<sup>6</sup>, L. Albert<sup>6</sup>, X. Delfosse<sup>1</sup>, F. Allard<sup>7</sup>, D. Homeier<sup>8</sup>, L. Malo<sup>7,9</sup>, C. Morley<sup>10</sup>, M. E. Naud<sup>7</sup>, and M. Bonnefoy<sup>1</sup>

<sup>1</sup> Univ. Grenoble Alpes, CNRS, IPAG, 38000 Grenoble, France  
e-mail: Philippe.Delorme@univ-grenoble-alpes.fr

<sup>2</sup> The University of Texas at Austin, Department of Astronomy, 2515 Speedway, Stop C1400, Austin, Texas 78712-1205, USA

<sup>3</sup> Carnegie Institution of Washington DTM, 5241 Broad Branch Road NW, Washington, DC 20015, USA

<sup>4</sup> Institut UTINAM, CNRS UMR 6213, Observatoire des Sciences de l'Univers THETA Franche-Comté Bourgogne, Univ. Bourgogne Franche-Comté, 41bis avenue de l'Observatoire, 25000 Besançon, France

<sup>5</sup> IfA, University of Hawai'i, 2680 Woodlawn Drive, Honolulu, HI 96822, USA

<sup>6</sup> Institut de Recherche sur les Exoplanètes, Université de Montréal, C.P. 6128, Succursale Centre-Ville, Montréal, QC H3C 3J7, Canada

<sup>7</sup> Univ. Lyon, ENS de Lyon, Univ. Lyon1, CNRS, Centre de Recherche Astrophysique de Lyon UMR 5574, 69007 Lyon Cedex 07, France

<sup>8</sup> Zentrum für Astronomie der Universität Heidelberg, Landessternwarte, Königstuhl 12, 69117 Heidelberg, Germany

<sup>9</sup> Canada-France-Hawaii Telescope Corporation, 65-1238 Mamalahoa Highway, Kamuela, HI96743, USA

<sup>10</sup> UC Santa Cruz, ISB 159/1156 High St, Santa Cruz, CA 95060, USA

Received 1 September 2016 / Accepted 1 March 2017

## ABSTRACT

**Aims.** We conducted a multi-wavelength, multi-instrument observational characterisation of the candidate free-floating planet CFBDSIR J214947.2–040308.9, a late T-dwarf with possible low-gravity features, in order to constrain its physical properties.

**Methods.** We analysed nine hours of X-shooter spectroscopy with signal detectable from 0.8 to 2.3  $\mu\text{m}$ , as well as additional photometry in the mid-infrared using the *Spitzer* Space Telescope. Combined with a VLT/HAWK-I astrometric parallax, this enabled a full characterisation of the absolute flux from the visible to 5  $\mu\text{m}$ , encompassing more than 90% of the expected energy emitted by such a cool late T-type object. Our analysis of the spectrum also provided the radial velocity and therefore the determination of its full 3D kinematics.

**Results.** While our new spectrum confirms the low gravity and/or high metallicity of CFBDSIR 2149, the parallax and kinematics safely rule out membership to any known young moving group, including AB Doradus. We use the equivalent width of the K I doublet at 1.25  $\mu\text{m}$  as a promising tool to discriminate the effects of low-gravity from the effects of high-metallicity on the emission spectra of cool atmospheres. In the case of CFBDSIR 2149, the observed K I doublet clearly favours the low-gravity solution.

**Conclusions.** CFBDSIR 2149 is therefore a peculiar late-T dwarf that is probably a young, planetary-mass object (2–13  $M_{\text{Jup}}$ , <500 Myr) possibly similar to the exoplanet 51 Eri b, or perhaps a 2–40  $M_{\text{Jup}}$  brown dwarf with super-solar metallicity.

**Key words.** brown dwarfs – planets and satellites: gaseous planets – stars: atmospheres – methods: observational – techniques: spectroscopic

## 1. Introduction

Brown dwarfs and giant exoplanets populate the same temperature range and share many physical properties, such as their molecule-dominated atmospheres and gradual cooling from ~3000 K at formation to ~100 K like the solar system gas-giant planets. Recent discoveries of very massive planets

(Chauvin et al. 2005; Marois et al. 2010; Delorme et al. 2013), some possibly more massive than the 13  $M_{\text{Jup}}$  deuterium burning mass limit, hint that planets could overlap with brown dwarfs in mass. On the other hand, the discovery of isolated L dwarfs in young clusters (Zapatero Osorio et al. 2002, 2014; Peña Ramírez et al. 2012), in young moving groups (Liu et al. 2013; Gagné et al. 2015; Gauza et al. 2015), and very cold very nearby Y dwarf objects (e.g., Kirkpatrick et al. 2012; Luhman 2014) show that very low-mass isolated brown dwarfs exist and overlap with the planetary masses. When these low-mass brown dwarfs are close enough and bright enough to be observed spectroscopically their atmospheres are much easier to study than similar exoplanets that lie near their very bright host stars. Liu et al. (2013) notably showed that the ~8  $M_{\text{Jup}}$  brown dwarf PSO J318.5–22, a  $\beta$ -pictoris moving group member

\* Based on observations obtained with X-shooter on VLT-UT2 at ESO-Paranal (run 091.D-0723). Based on observations obtained with HAWKI on VLT-UT4 (run 089.C-0952, 090.C-0483, 091.C-0543, 092.C-0548, 293.C-5019(A) and run 086.C-0655(A)). Based on observations obtained with ISAAC on VLT-UT3 at ESO-Paranal (run 290.C-5083). Based on observation obtained with WIRCcam at CFHT (program 2012BF12). Based on *Spitzer* Space telescope DDT observation (program 10166).

\*\* NASA Sagan fellow.

shares the spectral characteristics of the young directly imaged exoplanets, as well as atypically red late-L spectral type objects (e.g., Faherty et al. 2013; Gizis et al. 2015; Kellogg et al. 2016; Schneider et al. 2014, 2016; Bonnefoy et al. 2016). When CFBDSIR J214947.2–040308.9, hereafter CFBDSIR 2149, was identified (Delorme et al. 2012), it seemed to be a candidate member of the AB Doradus young moving group and, together with the low-gravity features in its spectrum, made it a unique T-type isolated planetary-mass candidate. Another earlier-type, isolated young planetary-mass T-dwarf, SDSS J111010.01+011613.1, has been identified as a bona fide member of AB Doradus moving group ( $149_{-19}^{+51}$  Myr; Bell et al. 2015) by Gagné et al. (2015). The late-T spectral type of CFBDSIR 2149 is typical of the coolest known directly imaged exoplanets, such as GJ 504 b or 51 Eri b (Kuzuhara et al. 2013; Macintosh et al. 2015), that the latest generation of adaptive optics systems are detecting. We therefore carried out a multi-wavelength, multi-instrument follow-up of CFBDSIR 2149 to fully characterise it and constrain its nature.

In Sect. 2 we present the new observations of CFBDSIR 2149, and in Sect. 3 we discuss the possible membership of CFBDSIR 2149 to young moving groups using updated kinematic data. In Sect. 4, we analyse the atmospheric properties that are compatible with this new spectral information, and in Sect. 5 we combine the spectral information, absolute flux measurement and dynamical information to assess several hypotheses on the physical nature of this peculiar late-T object. While we explore in the following the possible surface gravities that can be compatible with the observed spectrum of CFBDSIR 2149, we use the adjectives “low”, “intermediate” and “high” gravity. For clarity and consistency, we systematically use the term “low gravity” to refer to all scenarios that would correspond to CFBDSIR 2149 firmly belonging to the planetary mass range, “intermediate” to refer to all scenarios that would lead to a mass at the planet/brown dwarf boundary and “high” to refer to all gravity clearly associated to brown dwarf masses. In practicality, this means  $\log g = 3.5$  and  $4.0$  are “low” gravity,  $\log g = 4.5$  is “intermediate” and  $\log g = 5.0$  and  $5.5$  are “high” gravity.

## 2. New observations of CFBDSIR 2149

### 2.1. Spectroscopy

We measured the flux emitted by CFBDSIR 2149 from  $0.6\ \mu\text{m}$  to  $2.4\ \mu\text{m}$  using nine hours of X-shooter (Vernet et al. 2011) observations acquired over several weeks in service mode, resulting in an on-source effective integration time of seven hours. We used a slit  $0.9''$  wide both in the visible and near-infrared (NIR), with a resolution of 8800 and 5300 in the visible and NIR, respectively. Individual exposures were 670 s in the visible and 234 s in the NIR. The seeing was better than  $1''$  and the airmass below 1.3.

The spectra were reduced using the latest ESO X-shooter pipeline (Modigliani et al. 2010), which produces two-dimensional, curvature-corrected, spectra from X-shooter’s NIR arm (from  $0.99$ – $2.5\ \mu\text{m}$ ) and visible arm (from  $0.6$ – $1.02\ \mu\text{m}$ ) for each Observing Block (OB). No signal was retrieved for wavelengths shorter than  $\sim 0.8\ \mu\text{m}$ , but a low signal-to-noise ratio (S/N) spectrum of the optical far-red was recovered from  $0.8$  to  $1.0\ \mu\text{m}$ . The trace was extracted with custom IDL procedures that used Gaussian boxes in the spatial dimension at each point along the spectral direction. The noise spectrum was obtained by measuring the dispersion among ten spectral pixels on a noise trace obtained by subtracting the science trace from itself after a 1-pixel shift. Since the shift is much smaller than

the full spectral resolution (4.2 pixels in the NIR and 6.0 pixels in the visible), this effectively removes the science spectrum, but keeps the information on the actual background and photon noise from the science trace.

The resulting one-dimensional (1D) spectra from all nine OBs were then divided by the telluric spectrum obtained from the observation of standard stars immediately after or immediately before each OB. These telluric spectra were reduced and extracted beforehand using the same pipeline as the science OBs. We then refined the spectral calibration for each OB by using the known spectral position of telluric features visible in the sky portion of the science data (i.e., the pixels on either side of the target’s spectrum). We also applied the correction for the barycentric velocity at this step so that the spectra for all OBs had the same velocity reference before stacking them. Since the data quality of each OB shows significant variation related to more or less optimal observing conditions, the individual spectra were finally combined weighting by the inverse variance. The same reduction and extraction procedures were used for the NIR and visible arms of X-shooter, but the S/N in the small common wavelength interval between the two arms is very low ( $S/N \sim 1$ ) and highly variable because it covers the transition from the dichroic sending all light to the VIS arm and the dichroic sending all light to the NIR arm. Within this small common wavelength intersection we selected the range where the signal to noise was better than 1.0 in each arm, and normalised the visible spectra so that the weighted average of the flux in this range was the same in both arms. Since we have no  $z'$ -band photometric detection of CFBDSIR 2149, we cannot calibrate the visible spectrum on photometry. We therefore caution that our scaling is not independently calibrated and might be affected by modest systematic errors. The S/N at full resolution ( $R \sim 5000$ ) on the  $J$ -band peak is approximately 15 per resolution element.

Though the X-shooter data reduction pipeline provides a flux-calibrated spectrum, we verified the flux homogeneity of this large wavelength coverage spectral data by comparing it with existing WIRCam and NTT photometry (see Table 2). We synthesised the science spectrum colours by integrating it multiplied by the WIRCam global transmission, including filter, instrument and telescope transmission and the detector quantum efficiency (see Sect. 2.2 of Delorme et al. 2008b, for details). We anchored these colours to the  $J$ -band photometry to obtain the spectrophotometric magnitudes. This test shows that the synthesised photometry agrees with our measurements within  $2\sigma$ , therefore validating the NIR absolute fluxes measured by X-shooter. As shown in Table 2, we also derived spectrophotometric  $CH_{4\text{on}}$  and  $CH_{4\text{off}}$  magnitudes from the spectra.

We used our X-shooter spectrum to derive the spectral indices defined in Burgasser et al. (2006), Warren et al. (2007), and Delorme et al. (2008a) that trace the strength of several molecular absorption features in T dwarfs. As shown in Table 1, the spectral indices are typical of a T7.5 dwarf, with a significantly enhanced  $K/J$  index, characteristic of relatively weak collision induced absorption by  $\text{H}_2$  (though greenhouse effect could participate to  $K$ -band flux enhancement, see Allard et al. 2012), and therefore imply a low-pressure photosphere (Leggett et al. 2002; Burgasser et al. 2004, 2006; Golimowski et al. 2004; Knapp et al. 2004). Hiranaka et al. (2012) propose an alternative explanation for the similarly red spectral energy distribution (SED) of some peculiar L-dwarfs, which could be caused by a thin dust layer above the photosphere. Since most of the dust is condensed in late-T dwarf photospheres, this alternative hypothesis is less likely for objects as cool as CFBDSIR 2149, making a low-pressure photosphere a more probable explanation for its

**Table 1.** Value of the NIR spectral indices of CFBDSIR 2149 (as defined by Burgasser et al. 2006; Warren et al. 2007; Delorme et al. 2008a) for some known late-T brown dwarfs.

Object	Sp. Type	H <sub>2</sub> O-J	W <sub>J</sub>	CH <sub>4</sub> -J	H <sub>2</sub> O-H	CH <sub>4</sub> -H	NH <sub>3</sub> -H	CH <sub>4</sub> -K	K/J
CFBDSIR 2149	T7.5	0.067	0.328	0.209	0.228	0.143	0.640	0.140	0.193
		±0.003	±0.005	±0.004	±0.007	±0.005	±0.005	±0.018	±0.003
SDSS1504+10	T7	T7.5	T7.5	T7.5	T7.5	T7.5	–	T6.5	–
		0.082	0.416	0.342	0.241	0.184	0.668	0.126	0.132
GI 570 D	T7.5	0.059	0.330	0.208	0.206	0.142	0.662	0.074	0.081
2M0415	T8	0.030	0.310	0.172	0.172	0.106	0.618	0.067	0.133
Ross458C	T8+	0.007	0.269	0.202	0.219	0.107	0.701	0.082	0.192
Wolf940B	T8+	0.030	0.272	0.030	0.141	0.091	0.537	0.073	0.111

**Notes.** Values were derived using spectra from this article and from Burgasser et al. (2006), Delorme et al. (2008a), Burningham et al. (2009, 2010).

**Table 2.** Photometry and spectrophotometry of CFBDSIR 2149 (using WIRCam/MegaCam filter set to generate synthetic colours).

Filter	Photometry	Spectrophotometry <sup>1</sup>
$z'_{ab}$ <sup>2</sup>	>23.2	23.96 ± 0.07
$Y^2$	20.83 ± 0.09*	20.88 ± 0.05
$J$	19.48 ± 0.04*	Reference
$H$	19.88 ± 0.06	19.76 ± 0.04
$K_S$	19.34 ± 0.05	19.44 ± 0.05
$CH_{4off}$	–	19.15 ± 0.04
$CH_{4on}$	20.7 ± 0.25*	20.57 ± 0.05
[3.6]	18.59 ± 0.07	–
[4.5]	17.07 ± 0.03	–

**Notes.**  $z'$  is in the AB system and all others are in the Vega system. <sup>(1)</sup> Spectrophotometry is anchored on  $J = 19.48 ± 0.04$  mag from WIRCam photometric measurements. <sup>(2)</sup> Spectrophotometry is possibly affected by small systematic uncertainties because of data rescaling below 1  $\mu\text{m}$ . (\*) From Delorme et al. (2012).

red  $J - K_s$  colour. Such low pressure could indicate a young, low-mass and therefore low-gravity object and/or of a more opaque, higher-altitude photosphere typical of a high-metallicity object.

## 2.2. Radial velocity

The spectral resolution of our X-shooter spectrum ( $R = 5300$ ) allowed us to measure the radial velocity of CFBDSIR 2149. As described above, our X-shooter data have been calibrated in velocity, with the barycentric correction applied. Any remaining shift in velocity between our observed spectrum and a properly calibrated reference spectrum would therefore be caused by their respective radial velocities. In order to use a reference with minimal noise, we used the best fitting BT-Settl model, with  $[M/H] = 0$ ,  $\log g = 3.5$  and  $T_{\text{eff}} = 700$  K as a reference. We converted the wavelength dimension into velocity and then cross-correlated the full model with our stacked spectrum of CFBDSIR 2149, taking into account the noise of the observations. We found that CFBDSIR 2149 has a radial velocity of  $8 ± 4$  km s<sup>-1</sup> with respect to the barycentre of the solar system. This measured radial velocity is discrepant at more than  $3\sigma$  with the velocity of a bona fide AB Doradus moving group member, strongly challenging the association to this moving group proposed in a previous publication (Delorme et al. 2012). As a sanity check, we derived the radial velocity of the T7.5 GI 570 D (Burgasser et al. 2000; McLean et al. 2003, 2007) using its NIRSPEC spectrum at  $R \sim 2500$  and the same approach. We found a radial velocity of  $22 ± 5$  km s<sup>-1</sup>, in good agreement with the radial velocity of

$26.8 ± 0.1$  km s<sup>-1</sup> derived by Nidever et al. (2002) for the much brighter primary GI 570 A.

## 2.3. NIR photometry

We also used the wide-field WIRCam imager ( $20' \times 20'$  Puget et al. 2004) at CFHT (run 12BF12) to obtain additional higher S/N photometry in  $H$  (800 s exposure time, on 2012-09-07, with 0.67'' seeing) and  $K_s$  bands (1360 s exposure time, on 2012-09-09 and 2012-10-10 with a seeing of 0.93'' and 0.46'') We used a modified version of the *jitter* utility within the ESO Eclipse package (Devillard 2001) to correct for the flat field, subtract the background, and co-add the exposures. We extracted photometry from the resulting images using point-spread-function fitting within *Source Extractor* (Bertin & Arnouts 1996) and calibrated the zero point using 2MASS (Skrutskie et al. 2006) stars within the same detector chip as the target; see Delorme et al. (2012) for more details. We obtained  $K_s = 19.34 ± 0.05$  mag and  $H = 19.88 ± 0.06$  mag, including calibration errors, therefore confirming the very blue  $J - H$  colour of  $-0.4$  mag typical of late-T dwarfs and the red  $J - K_s$  colour of  $+0.14$  mag, very atypical for a late-T dwarf (see Fig 1) and plausibly caused by low gravity or high metallicity.

## 2.4. Mid-infrared flux from Spitzer Space Telescope

Like all late-T dwarfs, CFBDSIR 2149 is expected to emit most of its flux in the thermal infrared, between 3–5  $\mu\text{m}$ . Obtaining photometric measurements of our targets in the mid-infrared was therefore key to constraining its bolometric luminosity. We initially tried to obtain these crucial photometric constraints in the 3–5  $\mu\text{m}$  range from the ground (5.5 h of VLT-ISAAC, run 290.C-5083), but a slightly above-average thermal background prevented us from achieving any detection during these deep ground-based observations (after a full reduction and analysis, we only derived a lower limit on the magnitude, with  $L > 15.7$  mag). CFBDSIR 2149 is not detected with WISE and is not in the *Spitzer* archive, so we obtained *Spitzer* observations (Program ID: 10166), in channel 1 (3.6  $\mu\text{m}$ , hereafter [3.6]) and channel 2 (4.5  $\mu\text{m}$ , hereafter [4.5]) of IRAC (Fazio et al. 2004). The data were acquired on 2014-09-02 and the target was clearly detected. We used the basic calibrated data provided by the *Spitzer* archive and MOPEX (MOsaicker and Point source EXtractor Makovoz & Marleau 2005) to create the mosaic and extract PSF-fitting photometry from our data. After 500 s exposure time in each channel, CFBDSIR 2149 was detected in channel 1 with  $S/N = 14.2$ , corresponding to a Vega magnitude

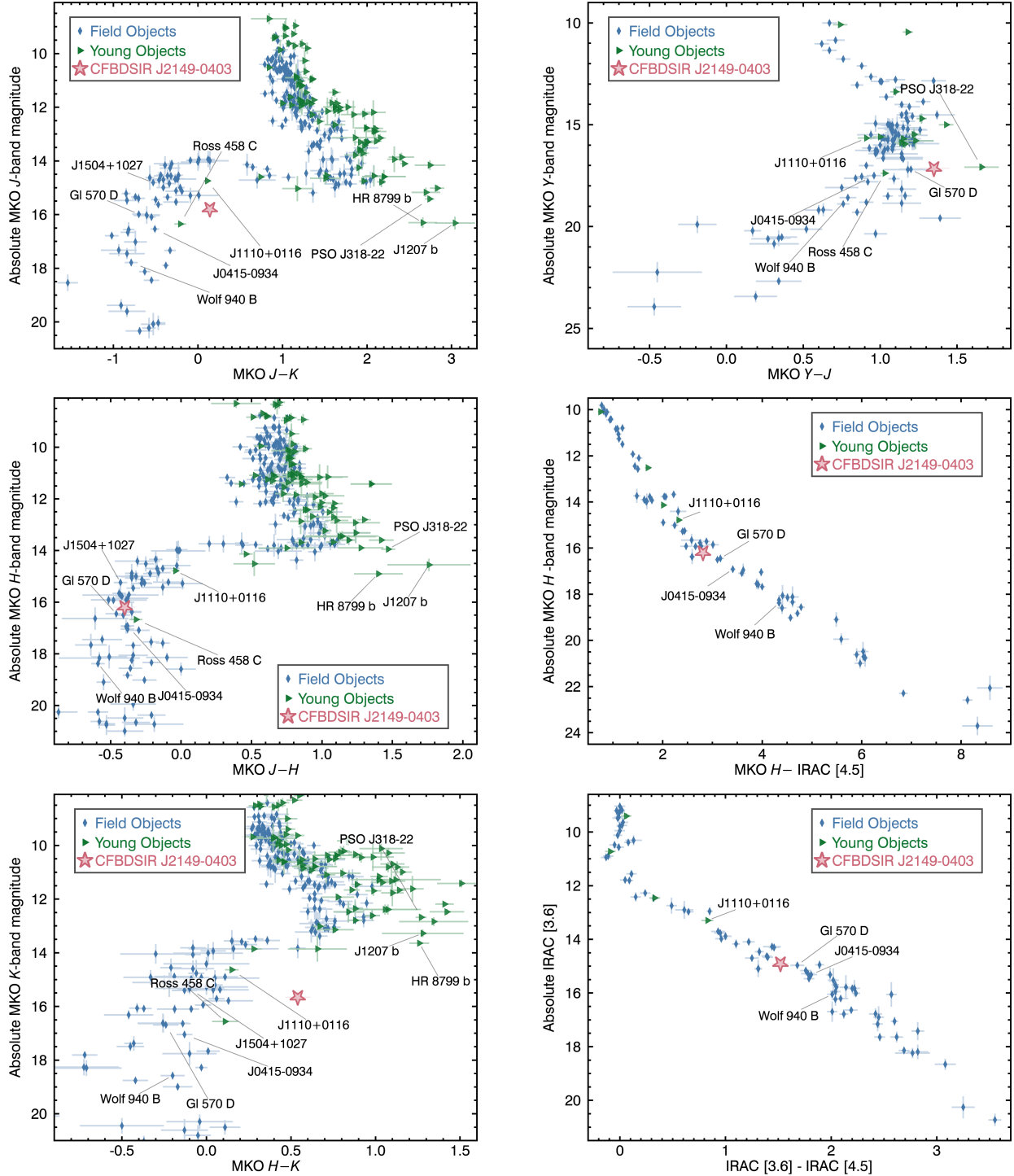


**Fig. 1.** Colours and absolute magnitudes of CFBDSIR 2149 (Red star) compared to known field and young L and T dwarfs.

of  $18.59 \pm 0.07$  mag, and in channel 2 with  $S/N = 54$ , corresponding to a Vega magnitude of  $17.07 \pm 0.03$  mag.

### 3. Parallax and kinematic analysis: exploring the membership of CFBDSIR 2149 to young moving groups

#### 3.1. Parallax and proper motion

We monitored CFBDSIR 2149 with the VLT facility near-infrared imager HAWK-I (Pirard et al. 2004; Casali et al. 2006; Kissler-Patig et al. 2008) in order to measure its parallax and

proper motion. We obtained nine dithered images in *J* band at each of 11 epochs over 2.05 yr beginning on 2012 Jun 26 UT. We centred the target on one detector of HAWK-I (field of view of  $3.6' \times 3.6'$  and a pixel scale of  $0.106''$ ). We reduced the images using the esorex pipeline (v1.8.13) using calibration data provided by the VLT archive to subtract darks, divide by a flat, and perform an iterative sky subtraction masking detected sources. Astrometric analysis of our images was performed in a similar manner as described in Dupuy & Liu (2012) and Dupuy & Kraus (2013). To correct non-linear distortion in the astrometry we interpolated the look-up table provided in

**Table 3.** Proper motion and parallax of CFBDSIR 2149.

Parallax (mas)	$1\sigma$ distance range (pc)	$\mu_\alpha$ (mas yr <sup>-1</sup> )	$\mu_\delta$ (mas yr <sup>-1</sup> )
$18.3 \pm 1.8$	49.8–60.6	$+138.3 \pm 1.2$	$-93.6 \pm 1.5$

the HAWK-I pipeline user manual version 1.9 (VLT-MAN-ESO-19500-4407). The astrometric reference grid was defined by 46 other stars in the field-of-view of the detector that CFBDSIR 2149 was centred on, 39 of which were in SDSS-DR9 (Ahn et al. 2012) and were used for the absolute calibration of the linear terms. The FWHM of the target was  $0''.68 \pm 0''.28$  (median and rms) with  $S/N = 20\text{--}50$  during our observations, which were constrained to be within 0.05 airmass of transit via timing constraints in the queue scheduling. Since the reference stars in the field have non-zero parallax and proper motion, we used the Besançon Galaxy model (Robin et al. 2003) to correct from this small effect (0.26 mas in parallax and  $-3$  mas/yr in proper motion) and obtain absolute measurements.

The absolute parallax and proper motion determined by MCMC are shown in Table 3 and Fig. 2, and the best-fit solution had a reduced  $\chi^2 = 1.08$ .

We also used the ten good quality astrometric epochs obtained under very good and homogeneous conditions to investigate the possible variability of CFBDSIR 2149 in  $J$  band. We selected a sample of 100 relatively bright and nearby stars located in the same HAWK-I detector as our target that we used as flux references. The resulting photometric error was 0.018 mag, including the calibration errors caused by the flux dispersion of the reference stars over all epochs, but dominated by error on the point source flux measurement of CFBDSIR 2149 itself. The measured photometric dispersion of CFBDSIR 2149 over all epochs was of 0.022 mag, therefore not significantly greater than the expected dispersion arising from photometric and calibration error alone. This rules out any strong photometric variability (i.e., above approx. 5%) in  $J$  band for our target over the ten epochs sampled by our parallax follow-up. However this constraint is too weak to rule out most of the photometric variations currently observed on brown dwarfs, which are usually of lower amplitude (e.g., Radigan 2014). We also note that the new photometric points in  $H$  and  $Ks$  are within  $1\sigma$  with respect to the photometry reported by Delorme et al. (2012).

### 3.2. Young moving group membership probability

We used the Bayesian Analysis for Nearby Young Associations II tool (BANYAN II Gagné et al. 2014) to update the probability that CFBDSIR 2149 belongs to any young moving group in the solar neighbourhood. We used its sky position, proper motion ( $\mu_\alpha \cos \delta = 138.3 \pm 1.2$  mas yr<sup>-1</sup>;  $\mu_\delta = -93.6 \pm 1.5$  mas yr<sup>-1</sup>), radial velocity ( $8 \pm 4$  km s<sup>-1</sup>) and trigonometric distance ( $54.6 \pm 5.4$  pc) as inputs to BANYAN II.

The new measurement of proper motion alone had the effect of favouring a membership to the  $\beta$  Pictoris moving group ( $\beta$ PMG) instead of the AB Doradus moving group (ABDMG), which was reported as most probable by Delorme et al. (2012) using the best measurements available at the time. However, both the trigonometric distance and radial velocity measurements that we present here reject a possible membership to all moving groups considered by BANYAN II (i.e., ABDMG,  $\beta$ PMG, Tucana-Horologium, Argus, Columba, Carina and TW Hydrae). The statistical distances and radial velocities associated with a membership to  $\beta$ PMG are  $24.1 \pm 2.0$  pc and  $-8.2 \pm 1.4$  km s<sup>-1</sup>,

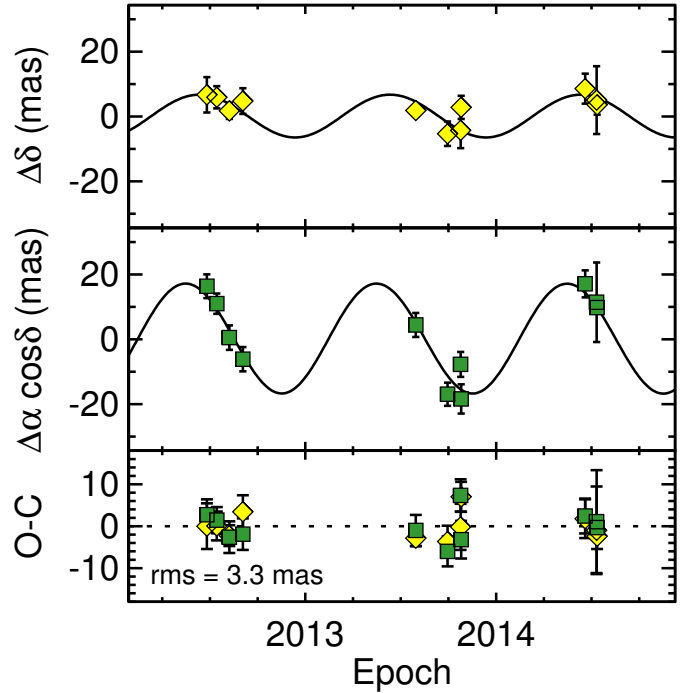


**Fig. 2.** The *top and middle panels* show relative astrometry in Dec ( $\delta$ ) and RA ( $\alpha$ ), respectively, as a function of Julian year after subtracting the best-fit proper motion. (This is for display purposes only; we fit for both the proper motion and parallax simultaneously in our analysis.) The *bottom panels* show the residuals after subtracting both the parallax and proper motion.

and those to ABDMG are  $38.6^{+2.0}_{-2.4}$  pc and  $-11.3 \pm 1.8$  km s<sup>-1</sup>, when using the updated proper motion measurement and treating radial velocity and distance as marginalised parameters (see Gagné et al. 2014, for a detailed explanation of the treatment of marginalised parameters).

Since we have obtained all measurements needed to compute the  $UVW$  space velocity ( $-12.8 \pm 2.4$ ;  $-18.2 \pm 3.2$ ;  $-38.0 \pm 4.0$ ), of CFBDSIR 2149, we can compare it directly with the position and kinematics of more young associations of stars not included in BANYAN II. As for Gagné et al. (2014), we used the formalism of Johnson & Soderblom (1987), with  $U$  positive toward the galactic centre,  $V$  positive toward the galactic rotation direction and  $W$  pointing upward from the galactic plane. The distance between CFBDSIR 2149 and the distribution mean of these various associations in spatial and kinematic spaces are presented in Fig. 3. We have included similar measurements for the moving groups considered in BANYAN II for comparison.

No known associations are located within  $26$  km s<sup>-1</sup> of CFBDSIR 2149, which corresponds to a minimal 3D Euclidian distance normalized by the  $UVW$  scatter of  $2.6\sigma$ , see Fig. 3. In particular, it can be noted that the  $W$  component ( $-38.0 \pm 4.0$  km s<sup>-1</sup>) of the space velocity of CFBDSIR 2149 taken alone is inconsistent with any known young association with a difference of at least  $24$  km s<sup>-1</sup>. This means that we have no robust dynamical age constraint that we could use as input for the study of the spectra and the atmosphere the object carried out in the following section. All of these considerations hold under the assumption that the young association member distributions follow normal distributions along each of the  $XYZUVW$  axes, that is, that there is no correlation between any combination of  $XYZUVW$ . For this reason, we used the BANYAN II moving

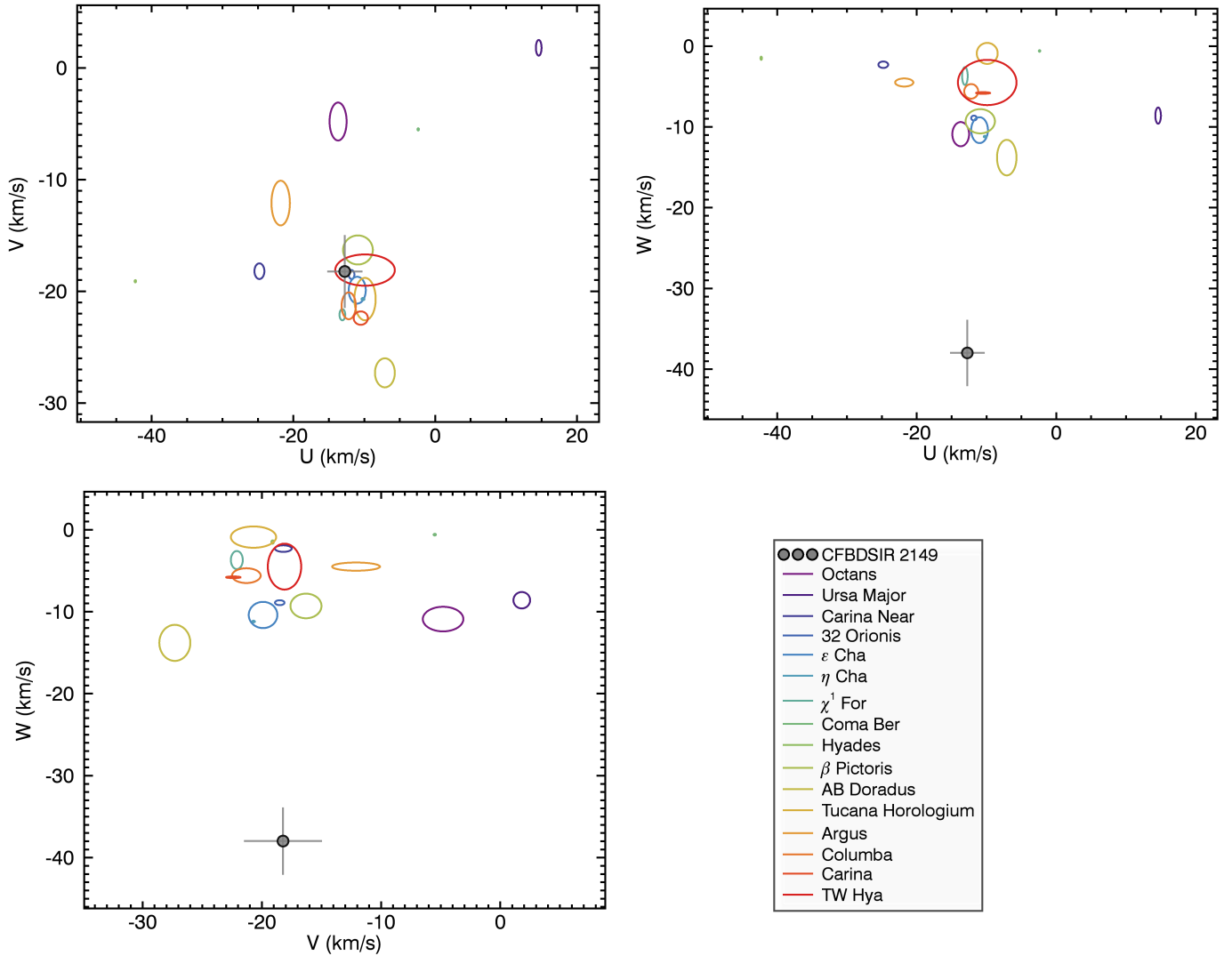


**Fig. 3.**  $U$ ,  $V$  and  $W$  velocities of CFBDSIR 2149 compared with the  $1\sigma$  ellipsoid velocity dispersion of the young moving groups considered in BANYAN II analysis.

groups central positions and scatters reported by Malo et al. (2013), since those were obtained using the same hypothesis (in contrast with those reported by Gagné et al. (2014) that allow for correlations between combinations of  $XYZ$  or  $UVW$  in the form of rotated Gaussian ellipsoid distributions).

#### 4. Atmospheric properties of CFBDSIR 2149: a spectral analysis

##### 4.1. Spectral synthesis

As a first step of the analysis of the atmospheric properties of CFBDSIR 2149, we performed a fit of our full X-shooter spectrum beyond  $0.8 \mu\text{m}$  and IRAC photometry against a grid of BT-Settl 2014 models (Allard 2014), examining effective temperatures from 500 K to 950 K with steps of 50 K and gravities from  $\log g = 3.5$  dex to 5.5 dex (cgs) with steps of 0.5 dex. We included both solar and super-solar metallicity models (+0.3 dex, i.e., approx. twice the solar abundance). We carried out a simple noise-weighted  $\chi^2$  minimisation fit on the full wavelength range, only excluding the range between 1.55 and  $1.59 \mu\text{m}$  where BT-Settl models lack the complete methane line list information

that has a significant impact on the emerging spectrum of late-T dwarfs (e.g., Canty et al. 2015). We also tried limiting the fit to the high-S/N emission peaks of our observed spectrum, but this did not affect the final results of the fit, therefore validating our noise-weighted fitting approach. However we do remove from the fit all data points with very low signal to noise (lower than 0.5) because they could include systematic errors, and contain negligible information. We first fitted the observed spectra to the models after normalising both observation and models to CFBDSIR 2149 the observed  $J$ -band peak between 1.255 and  $1.29 \mu\text{m}$ , which is a common approach in brown dwarf studies where parallaxes and hence absolute fluxes are not always available. We then fitted models and observations in absolute fluxes, which is much more constraining on models because they have not only to match the shape of the observed spectrum, but also its actual flux.

##### 4.1.1. Fitting models to observations after flux normalisation on the $J$ -band peak

The best fitting model normalised at  $J$  band was consistent with our “by-eye” fit and corresponded to a cool (700 K), low gravity

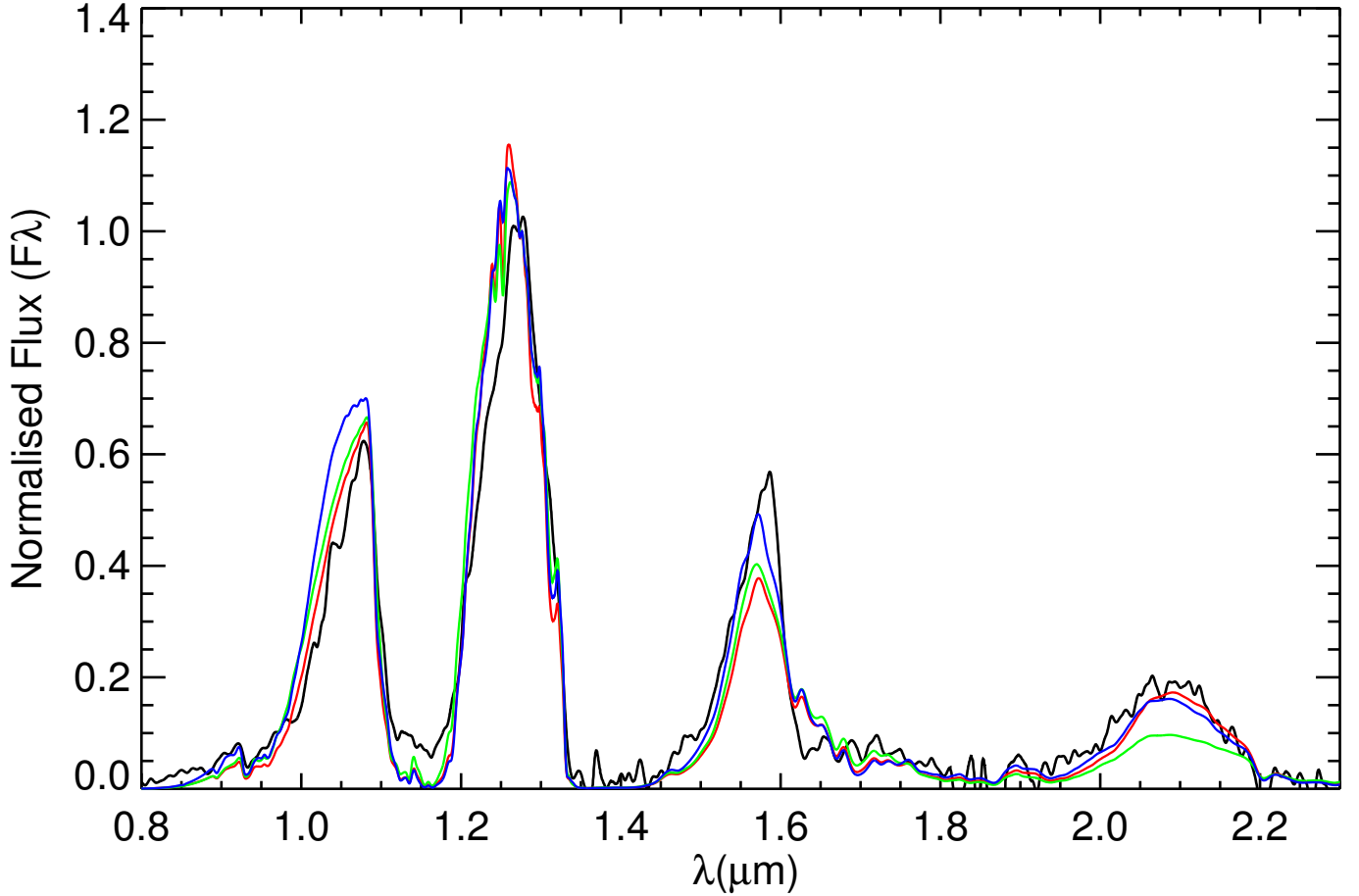


**Fig. 4.** Observed spectrum of CFBDSIR 2149 in black. Best fitting BT-Settl models after normalisation on the  $J$ -band peak flux are represented in colour. The spectra presented here have been binned to  $R \sim 200$  and are normalised on their  $J$ -band peak intensity. Blue: best fitting overall model (700 K,  $\log g = 3.5$ ,  $[M/H] = 0$ ). Red: best fitting model when high metallicity is forced (800 K,  $\log g = 4.5$ ,  $[M/H] = 0.3$ ). Green: best fitting model when high gravity and solar metallicity are forced (850 K,  $\log g = 5.0$ ,  $[M/H] = 0.0$ ).

( $\log g = 3.5$ ) atmosphere at solar metallicity, as shown in blue in Fig. 4. The largest discrepancies between this best fitting model and the observations are in the flux intensity in  $Y$ -band and in a slight shift in the position of the  $J$ -band peak, aside from missing  $\text{CH}_4$  absorption lines in the red part of the  $H$ -band peak due to an incomplete  $\text{CH}_4$  line list in BT-Settl. We also tried to force high metallicity ( $[M/H] = +0.3$ ) and high gravity ( $\log g \geq 5.0$ ) fits, whose best solutions are also shown in Figs. 4 and 7. The band by band higher resolution spectra of CFBDSIR 2149 and of the best fitting models are shown in Fig. 7. While the high-gravity solution shows significant discrepancies with respect to the observations in several bands, the high-metallicity solution has almost the same  $\chi^2$  as the low-gravity one and provides a much better fit in the  $Y$  band and a slightly better one in the  $K$  band. However the high-metallicity fit also favours moderate gravity ( $\log g = 4.5$ ) and leads to a higher effective temperature (800 K), resulting in underestimating the strength of  $\text{H}_2\text{O}$  and  $\text{CH}_4$  absorption in  $H$  band. The reduced  $\chi^2$  for the best fits are 1.72, 1.73 and 2.06 for the low-gravity, high-metallicity and field-gravity respectively.

#### 4.1.2. Fitting models to observations in absolute flux

After obtaining a reliable parallax for CFBDSIR 2149, we were able to directly compare its absolute flux at  $54.6 \pm 5.4$  pc to that of model atmospheres that would be located at the same distance.

Past studies of brown dwarf atmospheres have often shown that model fitting the shape of an observed spectrum sometimes falls orders of magnitude short of fitting its absolute fluxes, especially when looking at peculiar objects (e.g., Skemer et al. 2011). Since the BT-Settl model grid we used is built on the result of the Baraffe et al. (2003) evolutionary models, each spectra has a physically self-consistent effective gravity adapted to its mass and radius. These physical parameters are shown for the best fitting models in Table 6. In our case, the best fitting model in absolute flux ( $\chi^2 = 2.13$ ) is a 650 K, low gravity ( $\log g = 3.5$ ) atmosphere with supersolar metallicity ( $[M/H] = +0.3$  dex).

We made a 2D cubic interpolation of the  $\chi^2$  values of the relatively coarse models grid (steps of 50 K in effective temperature and 0.5 dex in  $\log g$ ) to provide a finer visualisation of the best fitting areas of the parameter range, both for solar metallicity and super solar metallicity models, see Fig. 6. After this interpolation, the best overall  $\chi^2$  (with a value of 1.97) would be for a 680 K, low gravity ( $\log g = 3.5$ ) solar metallicity object, quite close to the 700 K best fit after normalisation of the flux in the  $J$  band. This suggests a slightly lower effective temperature, at solar metallicity, might provide an even better fit to the data than the super solar metallicity solution, with the corresponding best fitting gravity unchanged at  $\log g = 3.5$  dex.

The overall  $\chi^2$  minima of the super-solar metallicity grid after interpolation ( $\chi^2 = 1.98$ ) is not itself at low gravity, but is located at 780 K for a gravity of  $\log g = 5.0$ . However, an

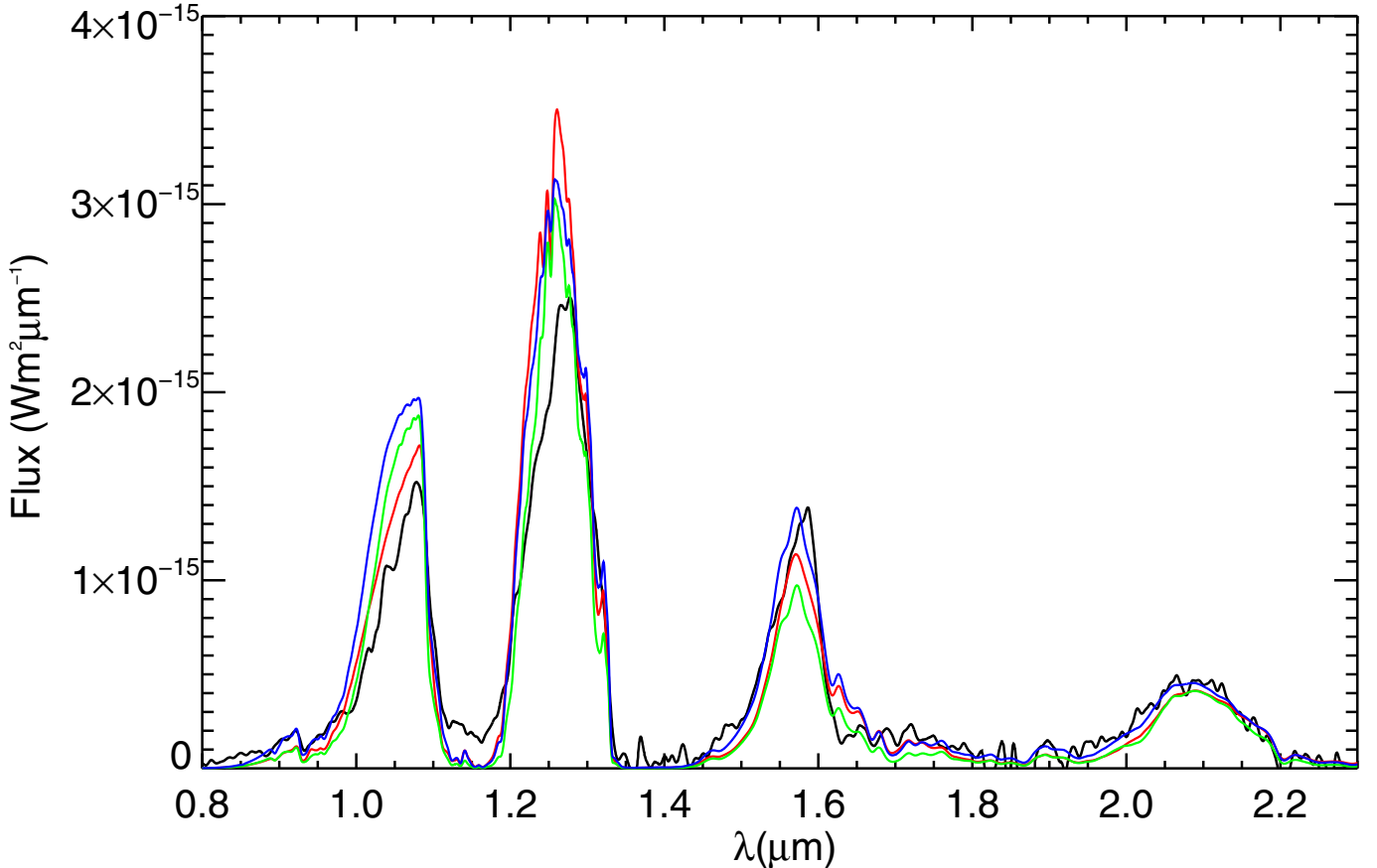


**Fig. 5.** Observed spectrum of CFBDSIR 2149 in black in each spectral band. Best fitting BT-Settl models in absolute flux ( $\text{W m}^2 \mu\text{m}^{-1}$ ) are represented in colour. The spectra presented here have been binned to  $R \sim 200$ . Blue: model closest to the best fitting solution in absolute flux after interpolation on both  $\chi^2$  maps (700 K,  $\log g = 3.5$ ,  $[\text{M}/\text{H}] = 0$ ). Red: model closest to the best fitting solution in absolute flux after interpolation on the high-metallicity  $\chi^2$  map (800 K,  $\log g = 5.0$ ,  $[\text{M}/\text{H}] = 0.3$ ). Green: best fitting model in absolute flux without interpolation (650 K,  $\log g = 3.5$ ,  $[\text{M}/\text{H}] = 0.3$ ).

important point to notice is that the super-solar metallicity  $\chi^2$  surface has several local minima, corresponding to several best fit solutions whose match to the data are good. This is caused by a degeneracy in  $T_{\text{eff}}/\log g$  when matching absolute fluxes: the same absolute flux can be matched by a larger radius (smaller  $\log g$ ) and a cooler effective temperature or by a smaller radius (larger  $\log g$ ) and warmer effective temperature. Since the absolute flux is a much steeper function of effective temperature than gravity, the temperature range that can match the absolute flux is approximately 150 K wide, from 650 to 800 K, while the corresponding matching  $\log g$  range spans almost two decades. This degeneracy in the model fitting is less marked for the solar metallicity models because the shape of the observed spectrum cannot be correctly matched at higher gravity, mostly because of the significant flux excess in the observed spectra in  $K$ . Even though the  $K$ -band data has a relatively low S/N, and a correspondingly lower weight in the fit, the discrepancy between the  $K$ -band flux of higher gravity models at solar metallicity and data is strong enough that higher gravity models are disfavoured and there is a global minima in the  $\chi^2$  surface for low gravity. In the case of the supersolar metallicity models, metallicity enhancement increases the opacity, which causes a higher altitude, lower pressure photosphere that can match the atypical SED of CFBDSIR 2149 in  $K$ -band even at higher gravity. Best fitting models at high-metallicity therefore correspond to a wide range of objects, from a young isolated planetary-mass object of a few  $M_{\text{Jup}}$ , to moderately old brown dwarfs of a few tens of  $M_{\text{Jup}}$ .

Since the local minima of the high-metallicity fit at low gravity basically describes the same type of object as the best fitting object at solar metallicity, a young planetary mass object, we will in the following consider mainly the best fit solution at high-metallicity, as a 800 K,  $\log g = 5.0$  intermediate mass brown dwarf, and the best fitting solution at solar metallicity as a 700 K,  $\log g = 3.5$ , young planetary mass object, as shown in Fig. 5. This allows us to investigate a truly distinct alternative when discussing the nature of CFBDSIR 2149.

Although such a comparison with BT-Settl atmosphere models suggests that CFBDSIR 2149 is not a field gravity object at solar metallicity, it cannot discriminate by itself between a low-gravity, solar metallicity atmosphere and a metal-enriched atmosphere. Finally we note that the main discrepancies in absolute flux between the low-gravity model and the observations are a significant lack of observed flux in the  $J$  band and even more so in the  $Y$  band, which could be similar to the reddening observed for unusually red L dwarfs. This spectral peculiarity has been proposed to be linked to the presence of a high altitude dust haze in their atmosphere by Hiranaka et al. (2012, 2016) and Marocco et al. (2014). We note that interstellar extinction in the direction of our target ( $A_V = 0.095$  mag, integrated on the full line of sight Schlegel et al. 1998) cannot cause a noticeable reddening. However, such a reddening could also be caused by the presence of an inversion layer in the upper atmosphere, as proposed by Tremblin et al. (2015), who manage a good fit to the spectra of ROSS458C, which is quite similar to the spectra

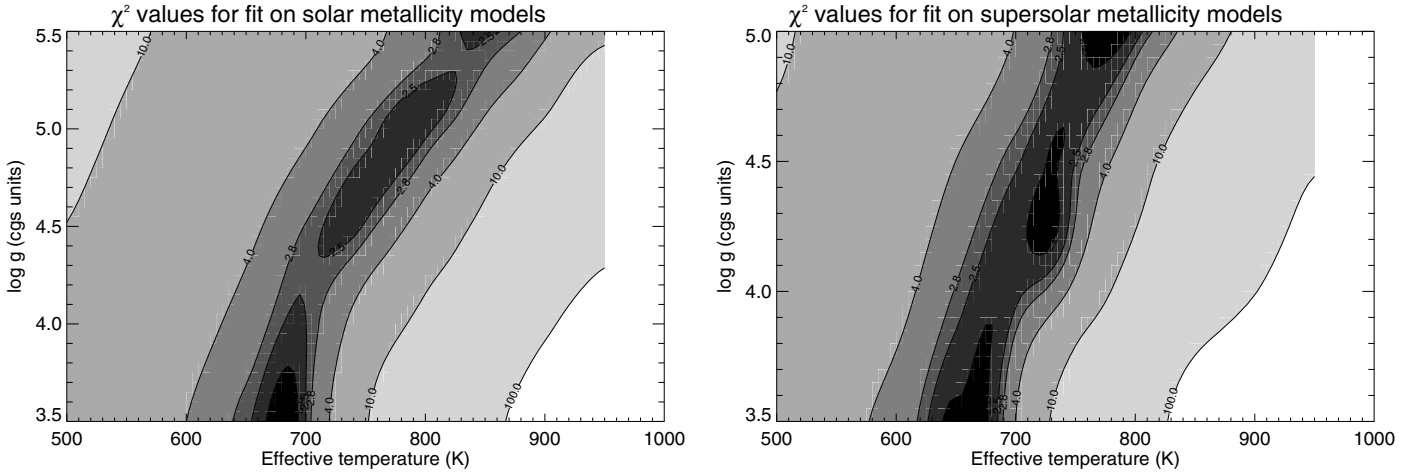


**Fig. 6.** Reduced- $\chi^2$  contour maps for the fit of the observed spectra in absolute flux to the BT-Settl solar (*left*,  $[M/H] = 0$ ) and supersolar (*right*,  $[M/H] = +0.3$ ) metallicity models.  $\chi^2$  values between the model grid points have been interpolated. The black areas are the best fitting range of the parameter space, where  $\chi^2 < 2.2$ .

of CFBDSIR 2149 according to Delorme et al. (2012). However, we note that Fig. 1 of Tremblin et al. (2015) shows that super solar metallicity is necessary to match the very red  $J - K$  colour of ROSS458C. It appears the out of equilibrium chemical processes put forward by Tremblin et al. (2015) have only a minor impact on the  $K$ -band flux of late T objects and therefore cannot explain alone the atypical  $K$ -band flux of ROSS458C and CFBDSIR 2149.

#### 4.2. Potassium lines equivalent width

Since the effects of low gravity and high metallicity on the global SED of cool atmospheres are very similar, finding an observable spectral feature that respond differently to a variation of gravity or metallicity would be key to breaking the degeneracy between these two physical parameters. Potassium lines are in theory a very powerful proxy to investigate metallicity in cool atmospheres, because metallicity enrichment means more potassium in the atmosphere and results in strongly enhanced KI lines at constant effective temperature. We derived the equivalent widths of the KI lines around  $1.25 \mu\text{m}$  using the prescriptions detailed in McLean et al. (2003) and Faherty et al. (2014). We did not study the KI doublet around  $1.17 \mu\text{m}$  because there is almost no signal left in the spectra of late-T dwarfs in this area of high water absorption. For CFBDSIR 2149 we retrieved equivalent widths of  $1.4 \pm 0.6 \text{ \AA}$  and  $3.5 \pm 0.6 \text{ \AA}$  for each component of the  $J$ -band doublet, comparable to the equivalent widths found by McLean et al. (2003) using the same formalism for G1 570D (T7.5) and 2M0415 (T8), see Table 4. We also derived equivalent widths for the BT-Settl 2014 models that produced the best fit of the overall spectrum of CFBDSIR 2149 (see Sect. 4.1). Though the KI lines contribute negligibly to the overall  $\chi^2$  in the fit, the best fitting model with very low gravity ( $\log g = 3.5$ ) leads to the best agreement by far in KI equivalent widths.

The high gravity model that provides a relatively poor fit to the overall SED also has KI equivalent widths that are much higher than we observe. This is because the correspondingly higher effective temperature of the model leads to stronger KI absorption bands, as corroborated by observations. It is to be noted that the field-gravity late-T dwarfs shown on Table 4 have lower temperatures than the best fitting high gravity models here. While these objects (as well as cooler high gravity models) have KI equivalent widths in reasonable agreement

with those of CFBDSIR 2149, it has already been shown in Delorme et al. (2012) that their overall spectra is strikingly different from CFBDSIR 2149. They both have a lower flux in  $H$ -band and even more in  $K$ -band, a difference that would arise naturally from increased CIA absorption if these field objects had higher surface gravity than CFBDSIR 2149. In this respect it appears that field-gravity solutions can either approximately match the spectra in  $Y$ ,  $J$ , and  $H$  bands but significantly miss the observed potassium line width or match the lines and significantly miss the overall spectra.

The high metallicity model at 800 K, which fits the overall SED of CFBDSIR 2149 including its strong  $K$ -band flux, completely fails at reproducing the observed KI equivalent widths, both because of its higher effective temperature and because of its higher metallicity. In fact, even for the low effective temperature (650 K), high metallicity best fit, the equivalent widths of KI lines remain significantly higher than the observed values. These findings are not in contradiction – nor do they support – the analysis by Knapp et al. (2004), that claims that low-gravity increases the KI equivalent width. Indeed the low gravity best fit to CFBDSIR 2149 spectrum has a smaller KI equivalent width, because it also has a lower effective temperature than the high gravity best fit, not because of its lower gravity. It appears the effect on KI lines of a 100 K change in effective temperature or of 0.3 dex in metallicity is much stronger than any effect a decade or more of change in gravity at constant effective temperature could cause. If this modelled trend is confirmed by future observations of benchmark objects of known metallicity, this would provide an efficient way to discriminate low-gravity atmospheres from high-metallicity atmospheres, which otherwise present very similar spectral features in the NIR. Such a diagnostic would be critical in the study of imaged massive exoplanets, which are low-gravity and could also be metal-enriched depending on their formation. In the case of CFBDSIR 2149, the observed weak equivalent widths of the  $1.25 \mu\text{m}$  KI doublet favours the hypothesis of a solar-metallicity, low-gravity object.

#### 4.3. Spectral synthesis: exploring different atmosphere models

To explore whether or not our spectral synthesis conclusions were strongly dependent on the set of models used, we fitted our observational data to other available state-of-the-art models,

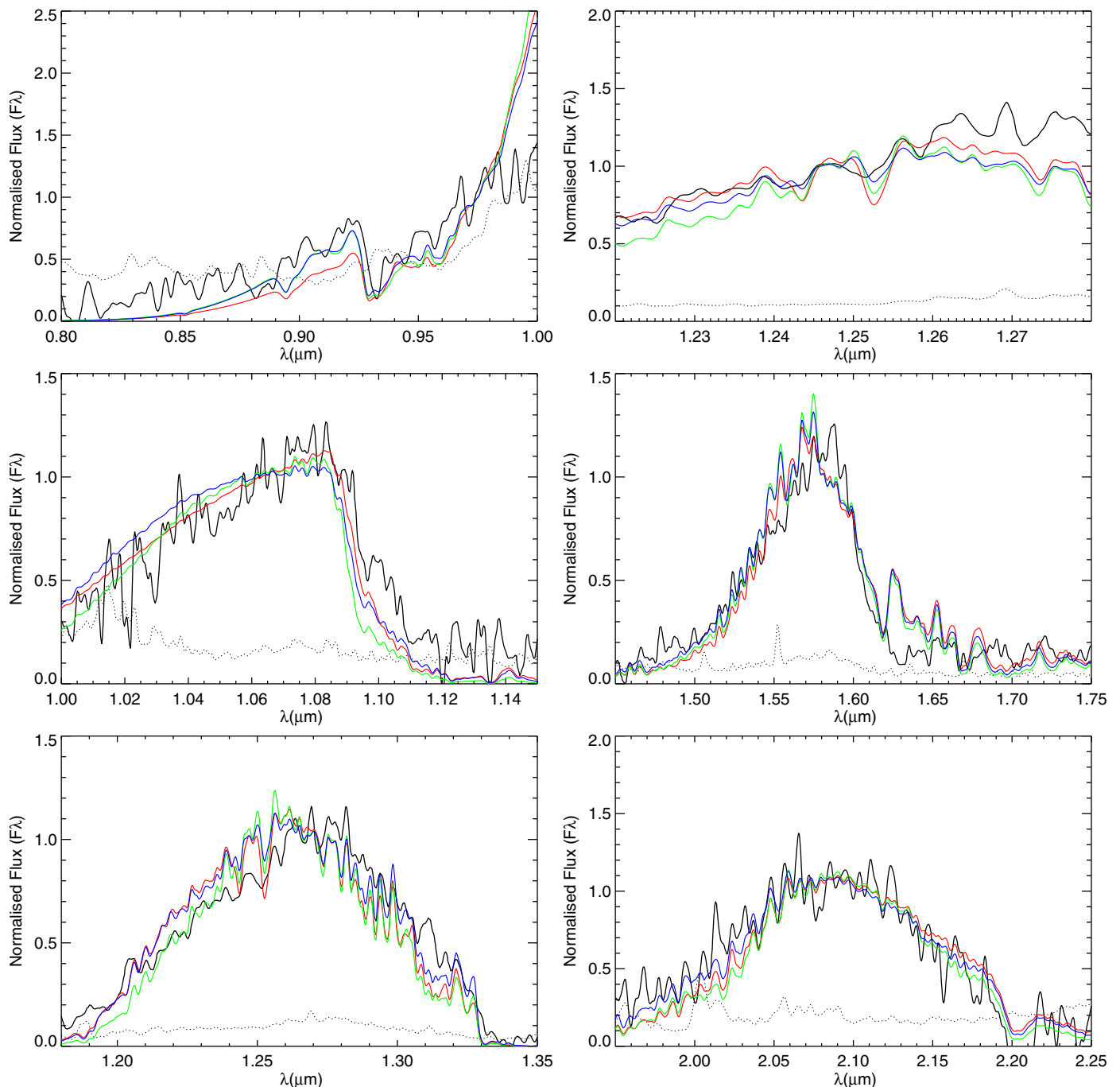


**Fig. 7.** Observed spectrum of CFBDSIR 2149 in black in each spectral band and around the KI doublet. Noise from the observed spectrum is represented by the black dotted line. *From top down and left to right* the panels show the spectra in  $z$  at  $R \sim 300$ , and at  $R \sim 600$  at all other wavelengths. The spectra presented here are normalised on their local peak intensity. Best fitting BT-Settl models in absolute flux are represented in colour. Blue: model closest to the best fitting solution in absolute flux after interpolation on both  $\chi^2$  maps (700 K,  $\log g = 3.5$ ,  $[M/H] = 0$ ). Red: model closest to the best fitting solution in absolute flux after interpolation on the high-metallicity  $\chi^2$  map (800 K,  $\log g = 5.0$ ,  $[M/H] = 0.3$ ). Green: best fitting model in absolute flux without interpolation (650 K,  $\log g = 3.5$ ,  $[M/H] = 0.3$ ).

starting with those of Burrows et al. (2003). This model grid has 32 spectra with effective temperatures and gravities self-consistently derived from evolutionary models (Burrows et al. 1997) for objects ranging from 1 to 25  $M_{\text{Jup}}$  and ages ranging from 100 Myr to 5 Gyr. The Burrows et al. (2003) model grid does not include super-solar metallicity objects and is relatively coarse, therefore it is possible that the real  $\chi^2$  minimum could be relatively far from any node of the model grid. However, it is interesting to note that the best fit ( $\chi^2 = 3.4$ ) corresponds to

a 7  $M_{\text{Jup}}$  free-floating planet aged 100 Myr, very similar to our BT-Settl results.

In order to make a more detailed comparison, we compared the data to atmosphere models similar to those described in Morley et al. (2012, 2014), which include opacities for sulfide and salt clouds that condense in T and Y dwarfs. The models we use here include two major updates to the opacities, including a new methane line list (Yurchenko & Tennyson 2014) and alkali line list (Allard et al. 2005). Chemical equilibrium calculations

**Table 4.** Equivalent width (in Å) of potassium lines at 1.243 and 1.254  $\mu\text{m}$ .

Object name or model parameters ( $\log g/T_{\text{eff}}/[M/H]$ )	Line 1	Line 2
CFBDSIR 2149 (T7.5p)	$1.4 \pm 0.6$	$3.5 \pm 0.6$
GI 570 D <sup>1</sup> (T7.5)	$1.7 \pm 0.6$	$2.6 \pm 0.8$
2M0415 <sup>1</sup> (T8)	$1.0 \pm 0.7$	$1.8 \pm 0.9$
3.5/700 K/[0.0] <sup>2</sup>	1.36	3.52
5.0/850 K/[0.0] <sup>3</sup>	4.26	7.94
4.5/800 K/[+0.3] <sup>4</sup>	6.33	10.84
3.5/650 K/[+0.3] <sup>5</sup>	2.36	5.60
5.0/800 K/[+0.3] <sup>6</sup>	5.84	10.56

**Notes.** <sup>(1)</sup> From McLean et al. (2003). <sup>(2)</sup> Best fitting BT-Settl model at low gravity. <sup>(3)</sup> Best fitting model at high gravity after flux normalisation. <sup>(4)</sup> Best fitting model at high metallicity after flux normalisation. <sup>(5)</sup> Best fitting model in absolute flux. <sup>(6)</sup> Best fitting model in absolute flux at high metallicity and high gravity.

(Lodders & Fegley 2006; Visscher et al. 2010) have also been revised and extended to include higher metallicities. These updates will be described in detail in a set of upcoming papers that focus on the new model grid (Marley et al., in prep.; Morley et al., in prep.; hereafter Ma&Mo2017).

Unlike BT-Settl, the Ma&Mo2017 model grid is not coupled with evolutionary models, so we cannot directly fit to our spectrum in absolute flux because there is no radius associated with a given atmosphere. The fits are therefore carried out after a normalisation in flux as described in Sect. 4.1.1. The resulting normalisation factor physically corresponds to assigning a radius to the object by scaling the flux of the model to the observed absolute flux of the object. Then, knowing the surface gravity of the model and the radius of the object, the mass of the object can be determined by applying Newton’s law. However, we adapted our fitting procedure so that it derives the radius corresponding to the flux (and gravity and mass) of the model. The only other modification of our fitting procedure with respect to what we used for the BT-Settl models is that we kept the *H*-band peak in the fit because the Ma&Mo2017 models use the latest methane line list, which enables a good fit in the *H* band. The grid covers temperatures from 450 to 900 K in steps of 25 K, with gravity ranging from 3.5 to 5.5 dex in steps of 0.5 dex and metallicities ranging from 0.0 to 1.0 dex in steps of 0.5 dex. Thus, the Ma&Mo2017 grid explores higher metallicities than the BT-Settl grid.

The overall best fitting model is a 900 K,  $\log g = 5.5$ , solar metallicity atmosphere ( $\chi^2 = 1.71$ ). Although this atmosphere completely fails at reproducing the *Y*-band peak and the *J*-band potassium doublet, it fits most of the data very well, notably in the high signal-to-noise part of the spectrum that has more weight in the  $\chi^2$  calculation. However, this atmosphere would correspond to a  $51 M_{\text{Jup}}$  brown dwarf with a radius of only  $0.66 R_{\text{Jup}}$ . According to the Cond evolutionary models of Baraffe et al. (2003), a  $50 M_{\text{Jup}}$  brown dwarf is expected to reach a temperature of approximately 900 K after 5 Gyr, with an expected radius of  $0.83 R_{\text{Jup}}$  that is much larger than the best-fit radius of  $0.66 R_{\text{Jup}}$ . In fact, the radius that fits the observed flux of CFBDSIR 2149 for this high-temperature model is also well below the minimum possible radius for any brown dwarf; even for an age of 10 Gyr the radius only reaches  $0.77 R_{\text{Jup}}$  for a  $72 M_{\text{Jup}}$  object. The minimum theoretical radius is governed by the well established physics of electron degeneracy pressure (Kumar 1963), so we reject this high-temperature, small-radius solution as unphysical. We note that the best-fit atmosphere with

900 K and  $\log g = 5.5$  would have a physically plausible radius if the flux were hypothetically higher due to a larger distance of at least 68 pc. This distance would correspond to a parallax of 14.7 mas, more than  $2\sigma$  smaller than our measured parallax of  $18.3 \pm 1.8$  mas.

If we remove the highest gravity  $\log g = 5.5$  dex models from consideration, the best fitting overall solution is a 775 K,  $\log g = 4.5$  dex solar metallicity atmosphere ( $\chi^2 = 1.96$ ). This model provides a much better fit in the *Y* and *H* bands (Fig. 8), but it is not as good in the *J* band as the previous solution. The radius and mass implied by this atmosphere are  $13 M_{\text{Jup}}$  and  $1.1 R_{\text{Jup}}$ , which almost exactly matches the substellar evolution models at 500 Myr for a  $13 M_{\text{Jup}}$  object.

If we force super-solar metallicity, we find the best fit is a 800 K,  $\log g = 5.0$  dex atmosphere ( $\chi^2 = 2.22$ ) with moderately high metallicity,  $[M/H] = +0.5$  dex, very similar to the best-fit solution of the BT-Settl model grid. The radius and mass corresponding to this atmosphere are  $0.87 R_{\text{Jup}}$  and  $35 M_{\text{Jup}}$ , in good agreement with Cond evolutionary model predictions for a 30–40  $M_{\text{Jup}}$  object at an age of 3 Gyr and a theoretical radius of approximately  $0.9 R_{\text{Jup}}$ . It is interesting to note that although the Ma&Mo2017 model grid does allow for a larger maximum metallicity of  $[M/H] = +1.0$  dex, the best high metallicity fit to our data is achieved using the intermediate step of  $[M/H] = +0.5$  dex.

Finally, forcing low gravity solutions also provides a good fit to the data ( $\log g = 4.0$ ,  $T = 775$  K,  $\chi^2 = 2.26$ ), associated with a radius of  $1.06 R_{\text{Jup}}$  and a mass of  $4.4 M_{\text{Jup}}$ . There is some tension with evolutionary model predictions that forecast that a 4–5  $M_{\text{Jup}}$  object cools down to 750–800 K for an age 40–50 Myr, with a larger radius of  $\sim 1.25 R_{\text{Jup}}$ . This would require CFBDSIR 2149 to be somewhat farther away, at a distance of  $\sim 65$  pc and  $1.6\sigma$  different from our parallax measurement, in order to be self-consistent. Though this low gravity solution is only marginally compatible with the measured absolute flux of the object, the continuity with the best overall fit, with the same effective temperature and  $\log g = 4.5$ , hints that a denser sampling in the models gravity grid could have revealed physically self-consistent solutions with good fit to the data for gravity between  $\log g = 4.0$  and  $\log g = 4.5$ . This range in gravity corresponds to masses between 5 and 13  $M_{\text{Jup}}$ . We also note that all of our fits converged toward either the fastest dust sedimentation speed (thinnest clouds) or to the *no cloud* setting (explicitly removing all dust from the atmosphere). Therefore, Ma&Mo2017 models strongly favour clear over dusty atmospheres.

After exploring model grids independent from BT-Settl, we conclude that the best-fit Ma&Mo2017 models are quite similar to those from BT-Settl. Two families of self-consistent solutions emerge, with the high-metallicity, high-gravity one being almost identical between the two model grids, having a temperature of 800 K, a gravity of  $\log g = 5.0$  dex and a moderate metallicity. The second family of plausible solutions indicates a relatively young planetary mass object. However the BT-Settl grid points toward cooler and lower gravity solutions, corresponding to objects well within the planetary mass range, while the Ma&Mo2017 models are consistent with objects slightly warmer, older and more massive, around  $13 M_{\text{Jup}}$ . Because of the higher effective temperatures none of these latter models can reproduce the very weak observed KI doublet at  $1.25 \mu\text{m}$  (Fig. 9). Thus, the potassium doublet would tend to favour the lower temperature found by the BT-Settl models, but on the other hand we note that the updated methane line list used by the Ma&Mo2017 models strongly improves the quality of the fit in the *J* and *H*-band peaks, possibly making this latter model

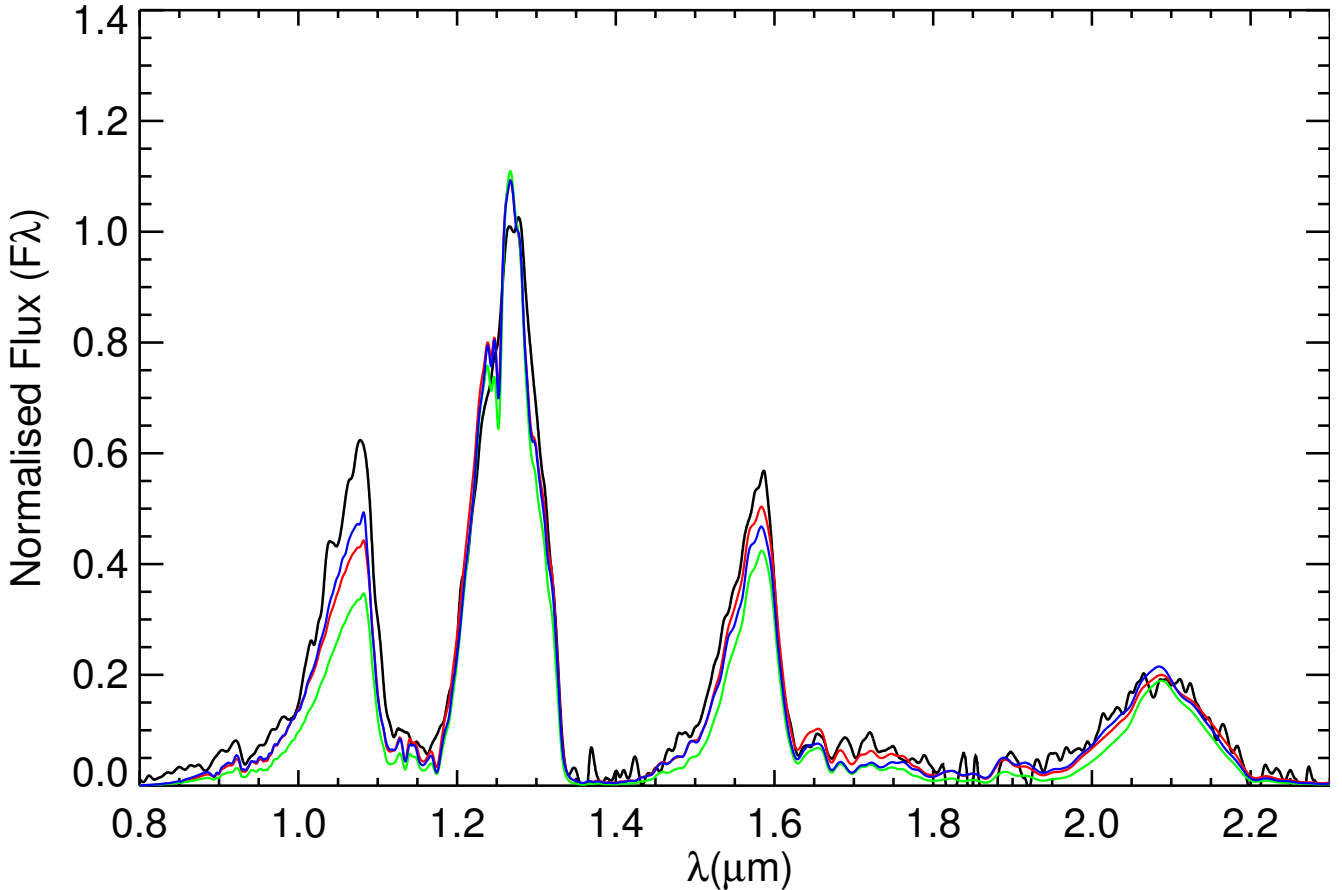


**Fig. 8.** Observed spectrum of CFBDSIR 2149 in black in each spectral band. Best fitting Ma&Mo2017 models after normalisation on the  $J$  band peak are represented in colour. The spectra presented here have been binned to  $R \sim 200$ . Blue: best fitting Ma&Mo2017 low-gravity model (775 K,  $\log g = 4.0$ ,  $[M/H] = 0$ ) Red: best fitting Ma&Mo2017 model (775 K,  $\log g = 4.5$ ,  $[M/H] = 0$ ). Green: best fitting Ma&Mo2017 high-metallicity model (800 K,  $\log g = 5.0$ ,  $[M/H] = +0.5$ ).

grid more reliable. It is encouraging to note that all the best-fitting Ma&Mo2017 models detailed in this section also correspond to local minima in the BT-Settl  $\chi^2$  maps, so perhaps the small differences between the two sets of best-fitting models arise partly from the different grid sampling rather than from different physics.

#### 4.4. Comparison with a known high-metallicity brown dwarf: GJ 758B

GJ 758B (Thalmann et al. 2009), GJ 504b (Kuzuhara et al. 2013) and Ross 458C (Burningham et al. 2011) are the only known late T-dwarfs with probable supersolar metallicity, making them prime benchmarks for comparison with CFBDSIR 2149. For all of these objects, other known late-T dwarf spectra and model spectra at high gravity and solar metallicity provide very poor fits to their atypical photometry. Since the age of GJ 504b is still unclear and its effective temperature is significantly lower (500–550 K Skemer et al. 2016) than CFBDSIR 2149, and since Ross 458C has already been compared to CFBDSIR 2149 in Delorme et al. (2012), we focus our comparison on GJ 758B. The primary GJ 758 is older than 600 Myr and has a metallicity  $[Fe/H] = 0.18 \pm 0.05$  (Vigan et al. 2016). In Fig. 10 and Table 5, we show normalised narrow-band photometry of GJ 758B (T8, Vigan et al. 2016) together with the corresponding spectrophotometry of CFBDSIR 2149. We see that the colours of GJ 758B agree well with those of

CFBDSIR 2149 in the  $J$  and  $H$  bands, as well as with the *Spitzer* photometry at  $4 \mu\text{m}$ , confirming the very similar spectral types of these objects. The photometry of GJ 758B differs from CFBDSIR 2149's spectra in the  $K$  band, hinting that moderately high metallicity alone cannot reproduce the very red SED of CFBDSIR 2149. Another discrepancy is visible in the  $Y$  band, with CFBDSIR 2149 being significantly bluer in  $Y - J$ , perhaps indicating that metallicity enhancement (by strengthening the alkali absorption) and high gravity (by extending the pressure-broadened wings of the very strong  $0.77 \mu\text{m}$  potassium doublet into the  $Y$  band) tend to blunt the  $Y$ -band flux in GJ 758B. It is striking that the SED of GJ 758B is distinct from that of CFBDSIR 2149 in ways that are qualitatively compatible with CFBDSIR 2149 having lower gravity than GJ 758B. Though these objects have colours that agree within  $2\sigma$  they have significantly different absolute luminosities see Table 5, with CFBDSIR 2149 being approximately five times brighter than GJ 758B. This large difference could only be explained by a combination of factors, such as a larger radius for CFBDSIR 2149, which would be consistent with low-gravity and a slightly higher effective temperature. It also opens the possibility that CFBDSIR 2149 could be an unresolved equal mass binary, but it also has to be noted that the flux of GJ 758B is highly unusual by itself (Vigan et al. 2016). Taken alone, such a comparison between only two objects cannot be conclusive, but it still tends to show that unusually low gravity might be at least partly responsible for the atypical spectral features of CFBDSIR 2149.

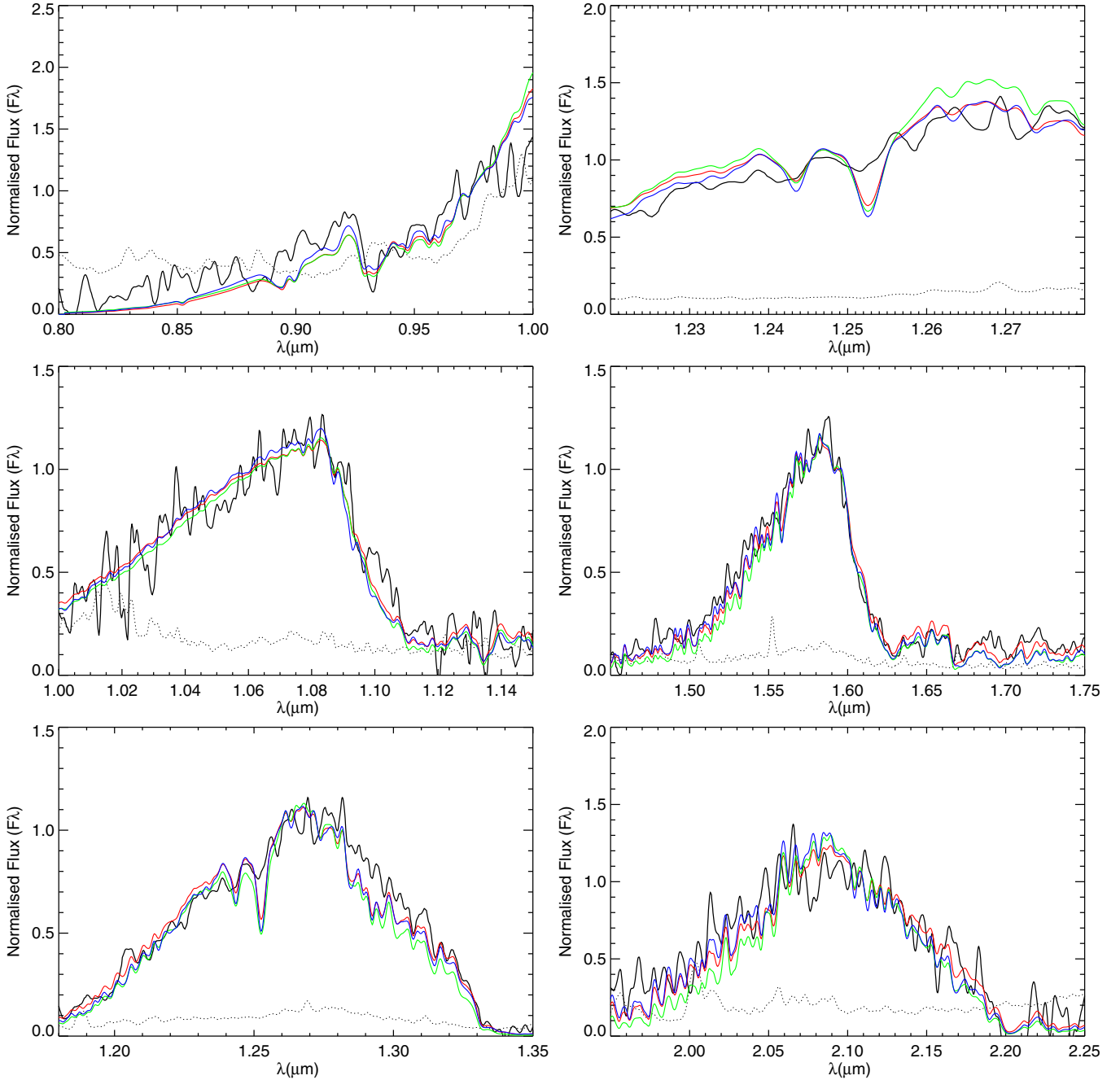


**Fig. 9.** Observed spectrum of CFBDSIR 2149 in black in each spectral band and around the KI doublet. Best fitting Ma&Mo2017 models after normalisation on the  $J$  band peak are represented in colour. Noise from the observed spectrum is represented by the black dotted line. *From top down and left to right* the panels show the spectra in  $z$  at  $R \sim 300$ , and at  $R \sim 600$  at all other wavelengths. The spectra presented here are normalised to their local peak intensity. Blue: best fitting Ma&Mo2017 low-gravity model (775 K,  $\log g = 4.0$ ,  $[M/H] = 0$ ) Red: best fitting Ma&Mo2017 model (775 K,  $\log g = 4.5$ ,  $[M/H] = 0$ ). Green: best fitting Ma&Mo2017 high-metallicity model (800 K,  $\log g = 5.0$ ,  $[M/H] = +0.5$ ).

#### 4.5. Bolometric flux

We converted the observed absolute fluxes into bolometric flux using the “super-magnitude” method described in Dupuy & Kraus (2013). In this approach, we combine fluxes calculated from  $J$ -,  $H$ -,  $[3.6]$ -, and  $[4.5]$ -band photometry into a magnitude defined as  $m_{JH12}$  by Dupuy & Kraus (2013), and for CFBDSIR 2149 we compute  $m_{JH12} = 19.292 \pm 0.025$  mag. Using the single bolometric correction of  $BC_{JH12} = 2.93 \pm 0.08$  mag derived by Dupuy & Kraus (2013) from the models of Morley et al. (2012), we find  $m_{\text{bol}} = 22.22 \pm 0.08$  mag. We note that by using only these bandpasses, and not including

$K$  band, the Dupuy & Kraus (2013) super-magnitude is more robust against assumptions about clouds and surface gravity. This can be seen in Fig. S4 of Dupuy & Kraus (2013) where, for example, the scatter in model-derived bolometric corrections at 700 K is small and primarily driven by surface gravity. In addition, the  $J - H$  colour of CFBDSIR 2149 is normal compared to field brown dwarfs, while its  $J - K$  colour is anomalously red, and Fig. 9 of Morley et al. (2012) shows that their models reproduce empirical  $J - H$  colour–magnitude diagrams. Therefore, we expect our super-magnitude approach to provide an accurate estimate of the bolometric magnitude of CFBDSIR 2149.

**Table 5.** Absolute magnitudes of CFBDSIR 2149 (synthesised from spectra) and GJ758B (observed), in the SPHERE narrow band filters.

	$M(Y2)$	$M(Y3)$	$M(J2)$	$M(J3)$	$M(H2)$	$M(H3)$	$M(K1)$	$M(K2)$
CFBDSIR 2149	$17.22 \pm 0.05$	$16.64 \pm 0.04$	$17.09 \pm 0.05$	$15.42 \pm 0.04$	$15.46 \pm 0.04$	$17.03 \pm 0.05$	$15.35 \pm 0.04$	$16.80 \pm 0.05$
GJ758b	$19.19 \pm 0.20$	$18.43 \pm 0.10$	$19.06 \pm 0.25$	$16.83 \pm 0.18$	$16.59 \pm 0.12$	$18.88 \pm 0.42$	$17.03 \pm 0.21$	$17.78 \pm 0.35$

**Notes.** The uncertainty on the parallax of CFBDSIR 2149 corresponds to an additional  $\pm 0.2$  mag systematic error.

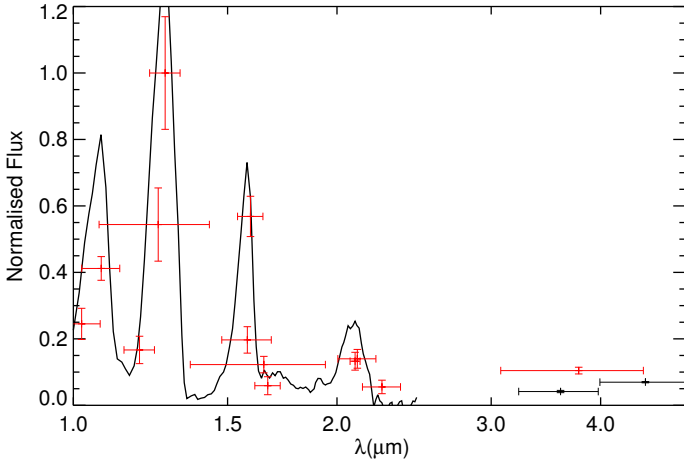


**Fig. 10.** Low-resolution spectra ( $R = 400$ ) of CFBDSIR 2149 (black) compared with the narrow band photometry of GJ 758B from Vigan et al. (2016), red crosses. Both data sets are normalised to their average flux in the  $J3$  filter.

Using our parallax of  $18.3 \pm 1.8$  mas, we compute a bolometric luminosity of  $\log(L_{\text{bol}}/L_{\odot}) = -5.51_{-0.09}^{+0.10}$  dex for CFBDSIR 2149. Given this luminosity and an assumption about the radius, we can compute a corresponding effective temperature for CFBDSIR 2149. Table 6 shows the corresponding effective temperatures associated with various age and mass hypotheses, using the solar metallicity *Cond* evolutionary tracks from Baraffe et al. (2003) to derive radius from mass and age.

#### 4.5.1. Comparison to BT-Settl atmosphere fits

To further assess the physical nature of CFBDSIR 2149, we compare our BT-Settl spectral fits to fundamental properties derived from evolutionary models given our measured luminosity and a range of possible ages (Table 6). The overall best fitting model spectrum ( $T_{\text{eff}} = 650$  K,  $\log g = 3.5$  dex,  $[M/H] = 0.3$ ) has  $\log(L_{\text{bol}}/L_{\odot}) = -5.42$  from its radius and effective temperature. This agrees relatively well with very young ages (20–50 Myr), corresponding to masses of  $\approx 2\text{--}5 M_{\text{Jup}}$ . The model spectrum at solar metallicity that is closest to the global  $\chi^2$  minimum, ( $T_{\text{eff}} = 700$  K,  $\log g = 3.5$  dex,  $[M/H] = 0$ ) has  $\log(L_{\text{bol}}/L_{\odot}) = -5.29$ , also agreeing best with very young ages and planetary masses. In this age range the effective temperatures expected from the bolometric luminosity are slightly lower, and the radius slightly smaller than the best fit on our model grid. However this slightly smaller radius and effective temperature are necessary to match the observed fainter bolometric luminosity of CFBDSIR 2149 and are well within the expected uncertainty of atmosphere models. Also we note that after interpolating  $\chi^2$  between the points of the discrete grid model, the overall  $\chi^2$  minimum consistently corresponds to a lower effective temperature ( $T_{\text{eff}} = 680$  K), associated with a fainter object.

Evolutionary models predict that by an age of 100 Myr the gravity reaches  $\log g = 4.06 \pm 0.04$  dex at a mass of  $6.4 \pm 0.6 M_{\text{Jup}}$ , which is one model grid step higher than the best fit value and thus perhaps marginally consistent. At older ages the solutions are, as expected, increasingly discrepant with the very low gravity hypothesis, which thus implies an age younger than approximately 100 Myr. The best-fit model atmosphere parameters when restricted to high metallicity ( $T_{\text{eff}} = 800$  K,  $\log g = 5.0$  dex,  $\log(L_{\text{bol}}/L_{\odot}) = -5.43$ ) are inconsistent with evolutionary model parameters at young ages but are consistent for ages of a few Gyr and corresponding masses of 20–40  $M_{\text{Jup}}$ . At ages older than this, gravity is significantly higher and at younger ages,  $T_{\text{eff}}$  is significantly cooler, constraining the age range within which the high-metallicity field gravity hypothesis is consistent to less than approximately 5 Gyr. Therefore, we conclude that both of the scenarios are self consistent within restricted age ranges from the perspective of evolutionary and atmosphere models. We also note that for an age of approximately 5 Gyr the best fit for high gravity (800 K,  $\log g = 5.0$ ,  $[M/H] = 0$ ,  $\log(L_{\text{bol}}/L_{\odot}) = -5.43$ ) is also consistent with the measured bolometric luminosity of CFBDSIR 2149. The main issue with this field-gravity hypothesis is that it significantly fails at reproducing the observed colours and spectra of CFBDSIR 2149.

#### 4.5.2. Comparison to Ma&Mo2017 atmosphere fits

The Ma&Mo2017 atmosphere models are independent of evolutionary models and thus have no a priori reason to be consistent with our bolometric flux measurements. However, the best overall fit of a 775 K, intermediate gravity ( $\log g = 4.5$ ), 13 Jupiter mass object with a radius of  $1.07 R_{\text{Jup}}$  is a very good match to the evolutionary model predictions of the observed bolometric flux of CFBDSIR 2149 for an age of 500 Myr; see Table 6. The high metallicity solution is very similar to the one obtained with BT-Settl, but with a smaller radius, consistent with an older age, closer to 5 Gyr. As highlighted in Sect. 4.3, both the low-gravity and the high-gravity Ma&Mo2017 atmosphere model best fits have associated radius that are too small, in significant disagreement with the observed absolute flux. When this is considered from the absolute bolometric flux point of view, this translates into a modelled effective temperature too high to match the evolutionary model predictions.

## 5. About the nature of CFBDSIR 2149

Though the large amount of data we collected clearly identify CFBDSIR 2149 as a peculiar late-T dwarf, it is more difficult to ascertain what kind of peculiar object it is. We therefore discuss in the following subsections the respective strengths and weaknesses of the four main hypotheses we envision.

### 5.1. CFBDSIR 2149 as young planetary mass object

The BT-settl model with solar metallicity, very low gravity ( $\log g = 3.5$ ), very large radius ( $1.53 R_{\text{Jup}}$ ) and a temperature of

**Table 6.** Effective temperature, gravity, mass and radius derived from the absolute luminosity of CFBDSIR 2149 for various age hypotheses and solar metallicity.

Age (Gyr)	$T_{\text{eff}}$ (K)	$\log g$	$M.(M_{\text{Jup}})$	$R.(R_{\text{Jup}})$
0.02	$675^{+35}_{-35}$	$3.58^{+0.04}_{-0.04}$	$2.6^{+0.3}_{-0.2}$	$1.271 \pm 0.007$
0.05	$685^{+35}_{-40}$	$3.85^{+0.04}_{-0.05}$	$4.3^{+0.4}_{-0.5}$	$1.231 \pm 0.001$
0.1	$695^{+35}_{-35}$	$4.06^{+0.04}_{-0.04}$	$6.4^{+0.6}_{-0.6}$	$1.176 \pm 0.001$
0.5	$735^{+30}_{-45}$	$4.42^{+0.01}_{-0.02}$	$12.3^{+0.3}_{-0.7}$	$1.066 \pm 0.003$
1.0	$765^{+45}_{-45}$	$4.74^{+0.04}_{-0.04}$	$20.9^{+1.7}_{-1.8}$	$0.979 \pm 0.009$
5.0	$845^{+50}_{-50}$	$5.25^{+0.04}_{-0.04}$	$47.0^{+3.0}_{-3.0}$	$0.811 \pm 0.008$
BT Models	$T_{\text{eff}}$ (K)	$\log g$	$M(M_{\text{Jup}})$	$R(R_{\text{Jup}})$
Low-g. <sup>1</sup>	700	3.5	2.7	1.53
Field 1 <sup>2</sup>	850	5.0	38	0.99
High-m.1 <sup>3</sup>	650	3.5	2.7	1.53
Field 2 <sup>4</sup>	800	5.0	38	0.99
High-m.2 <sup>5</sup>	800	5.0	38	0.99
Ma&Mo Models	$T_{\text{eff}}$ (K)	$\log g$	$M(M_{\text{Jup}})$	$R(R_{\text{Jup}})$
Low-g. <sup>6</sup>	775	4.0	4.3	1.06
Field <sup>7</sup>	900	5.5	51	0.66
High-m. <sup>8</sup>	800	5.0	35	0.87
Best fit <sup>9</sup>	775	4.5	13	1.07

**Notes.** <sup>(1)</sup> Best fitting BT-Settl model after normalisation at low gravity (700 K,  $\log g = 3.5$ ,  $[M/H] = 0$ ,  $\log(L_{\text{bol}}/L_{\odot}) = -5.29$ ). <sup>(2)</sup> Best fitting BT-Settl model after flux normalisation at high gravity (850 K,  $\log g = 5.0$ ,  $[M/H] = 0$ ,  $\log(L_{\text{bol}}/L_{\odot}) = -5.32$ ). <sup>(3)</sup> Best fitting BT-Settl model in absolute flux (650 K,  $\log g = 3.5$ ,  $[M/H] = +0.3$ ,  $\log(L_{\text{bol}}/L_{\odot}) = -5.42$ ). <sup>(4)</sup> Best fitting BT-Settl model in absolute flux at high gravity (800 K,  $\log g = 5.0$ ,  $[M/H] = 0$ ,  $\log(L_{\text{bol}}/L_{\odot}) = -5.43$ ). <sup>(5)</sup> Best fitting BT-Settl model in absolute flux at high metallicity (800 K,  $\log g = 5.0$ ,  $[M/H] = +0.3$ ,  $\log(L_{\text{bol}}/L_{\odot}) = -5.43$ ). <sup>(6)</sup> Best fitting Ma&Mo2017 model at low gravity (775 K,  $\log g = 4.0$ ,  $[M/H] = 0$ ). <sup>(7)</sup> Best fitting Ma&Mo2017 model at high gravity (900 K,  $\log g = 5.5$ ,  $[M/H] = 0$ ). <sup>(8)</sup> Best fitting Ma&Mo2017 model at high metallicity (800 K,  $\log g = 5.0$ ,  $[M/H] = +0.5$ ). <sup>(9)</sup> Best fitting overall Ma&Mo2017 model (775 K,  $\log g = 4.5$ ,  $[M/H] = 0$ ).

700 K is the solar metallicity model which provides the best fit of the spectrum and photometry of CFBDSIR 2149 (Fig. 4). Qualitatively, the low gravity strongly decreases the collision-induced absorption by  $\text{H}_2$  in the  $K$  band, explaining the red  $J - K$ s colour and the bright  $K$ -band absolute flux. The low temperature explains the blue  $J - H$  colour and the strong methane and water absorption band in the NIR spectra. The very large radius is necessary to account for the strong flux emitted by this object that appears much more distant and so intrinsically brighter than what would be expected for a field gravity object. Figure 1 shows the absolute magnitude of CFBDSIR 2149 compared to other field T dwarfs. The Dupuy & Liu (2012) polynomial fit to the absolute magnitude for a field brown dwarf of spectral type T7.5 is fainter by 0.3, 0.3 and 1.0 mag in  $J$ ,  $H$ , and  $K$  bands, respectively. CFBDSIR 2149 is thus significantly over-luminous only in  $K$  band. Even an earlier type T7 field brown dwarf is  $\sim 0.5$  mag less luminous in  $K$  band than CFBDSIR 2149. Our analysis in Sect. 4.5 using the bolometric luminosity also shows that a young-age hypothesis and planetary mass range (20 to 500 Myr) results in effective temperatures and radii that are in reasonable agreement with those derived in Sect. 4.1 from the comparison with atmosphere models. Both BT-Settl models and Ma&Mo2017 models best fit correspond to young planetary

mass objects, with the former favouring very young ages and masses of 2–7  $M_{\text{Jup}}$ , and the latter hinting at slightly older ages and heavier masses, up to 500 Myr and 13  $M_{\text{Jup}}$ . We caution that temperatures derived from fitting model atmospheres to normalised spectra and those derived using luminosities and evolutionary model radii do not always quantitatively agree for late-T dwarfs (e.g., Dupuy & Kraus 2013). Therefore, CFBDSIR 2149 could be somewhat younger or older than we find through this comparison of temperatures, depending on the level of systematic error in the models.

Still, two other independent points raised during our analysis also support a low-gravity in the atmosphere of CFBDSIR 2149. The first is the equivalent width of the  $K_1$  doublet at 1.25  $\mu\text{m}$  that agrees much better with the best fitting low-gravity model than with higher-gravity or higher-metallicity models. The second is the comparison with the companion GJ 758B whose age (and hence field-gravity  $\log g = 5.0$ –5.5) and slightly super-solar metallicity is known from its main sequence G-type host star. Although the two objects have the same spectral type, the SED of GJ 758B and CFBDSIR 2149 differ significantly in bands where gravity strongly influences the emergent flux (in  $K$  band by collision-induced absorption of  $\text{H}_2$ , and in  $Y$  band by the pressure broadened red wing of the 0.77  $\mu\text{m}$   $K_1$  doublet). These differences in both  $Y$  and  $K$  bands tend to show that CFBDSIR 2149 has a lower gravity than GJ 758B, while their very similar colours in  $J - H$  confirm that they have similar effective temperatures. The fact that CFBDSIR 2149 is more luminous than GJ 758B would therefore also be consistent with CFBDSIR 2149 having a larger radius (and lower gravity) than GJ 758B. Finally, we note that models with both high metallicity and low gravity actually provide the best fit to the data, making it plausible that CFBDSIR 2149 could be a metallicity-enhanced isolated planetary-mass object.

The main weakness of the young age hypothesis is the lack of any independent age estimation for CFBDSIR 2149, especially because the kinematic data we present in this article clearly show that it is not a member of any known young association. Though isolated young objects exist in the solar neighbourhood, they are rare.

## 5.2. CFBDSIR 2149 as an isolated analog to 51 Eri b

The lower end of our inferred age range for CFBDSIR 2149 (20–100 Myr) is consistent with that of the recently discovered exoplanet 51 Eri b (Macintosh et al. 2015) that is a member of the  $\beta$  Pictoris young moving group ( $24 \pm 3$  Myr; Bell et al. 2015). Table 7 recapitulates the published NIR photometry of 51 Eri b and compares it with CFBDSIR 2149, which appears to be 0.7–1.0 mag brighter in absolute flux in  $J$  and  $H$  bands. According to the “hot start” Cond models, such a flux difference at a fixed age of 20 Myr would correspond to masses of 2  $M_{\text{Jup}}$  for 51 Eri b and 3  $M_{\text{Jup}}$  for CFBDSIR 2149. They could even share the same mass if CFBDSIR 2149 were an unresolved, equal-mass binary, but observational evidence does not currently exist to support or fully disprove such a hypothesis. The  $J - H$  colours of 51 Eri b and CFBDSIR 2149 match within  $1\sigma$ , which is indicative that these objects might share a similar SED, but this constraint is not very strong because the error bars on the 51 Eri b photometry are very large. A new analysis of  $K$ -band data of 51 Eri b from SPHERE, however, suggests it also shares with CFBDSIR 2149 an atypically red  $J - K$  colour (Samland et al. 2017). Since young L-type exoplanets are usually underluminous in the NIR compared to older objects with a similar effective temperature (e.g., Skemer et al. 2011); the similar colours and higher luminosity

**Table 7.** Absolute magnitudes and  $J - H$  colour of CFBDSIR 2149 and 51 Eri B

	$M(J)$	$M(H)$	$J - H$
CFBDSIR 2149 <sup>1</sup>	$15.78 \pm 0.04$	$16.14 \pm 0.06$	$0.36 \pm 0.07$
51 Eri B <sup>2</sup>	$16.75 \pm 0.40$	$16.86 \pm 0.21$	$0.11 \pm 0.45$

**Notes.** <sup>(1)</sup> The uncertainty on the parallax of CFBDSIR 2149 corresponds to an additional  $\pm 0.2$  mag systematic error. <sup>(2)</sup> From Macintosh et al. (2015).

of CFBDSIR 2149 could be consistent with it being older than 20 Myr and more massive than 51 Eri b. However, it is unclear whether such a trend exists for T spectral types, and the only known young T dwarf with a parallax and a well established age SDSS J111010.01+011613.1, a member of AB Doradus ( $149^{+51}_{-19}$  Myr; Bell et al. 2015), shows no such underluminosity (Gagné et al. 2015). Overall, the hypothesis that CFBDSIR 2149 is a slightly more massive analogue to 51 Eri b is compatible with our derived mass and age range for CFBDSIR 2149 and with the available data for 51 Eri b, which may be even redder in  $J - K$  than CFBDSIR 2149 given that it likely has a lower gravity.

### 5.3. CFBDSIR 2149 as relatively young super-solar metallicity brown dwarf

High-metallicity model atmospheres at moderate gravity provide as good a  $\chi^2$  as the low gravity ones, so it is plausible that CFBDSIR 2149 could be relatively young with super-solar metallicity. This hypothesis is also consistent with our comparison of CFBDSIR 2149 to the slightly super-solar metallicity, field gravity ( $\log g = 5.0-5.5$ ) T dwarf GJ 758B. Their SEDs disagree but could perhaps be brought into qualitative agreement if CFBDSIR 2149 has a moderately lower gravity ( $\log g = 4.5-5.0$ ). The main observational evidence that is not compatible with CFBDSIR 2149 being a relatively young super-solar metallicity brown dwarf is its relatively weak KI doublet at  $1.25 \mu\text{m}$  that models predict would be much stronger if the object were metal enriched. However, the reliability of atmosphere models in this poorly constrained temperature and metallicity range is not yet established, and direct comparison with the KI doublet of GJ 758B is not possible because of the lack of resolved spectroscopic data for this close companion. Independently of these considerations, a significant issue with this hypothesis is that high metallicity objects are very rare, with Boone et al. (2006) finding that less than 1% of objects in the solar neighbourhood have  $[M/H] > 0.2$ .

### 5.4. CFBDSIR 2149 as a peculiar unresolved binary

Brown dwarfs with atypical colours and/or spectral features can sometimes be explained by unresolved binarity (e.g., Bardalez Gagliuffi et al. 2014) when the fainter unresolved companion makes a significant contribution at some wavelengths while most of the combined-light spectrum is representative of the brighter primary. In the case of CFBDSIR 2149 the atypical flux excess is in the  $K$  band where the flux is supposed to decrease with temperature in the T dwarf range. This implies a higher temperature and a higher  $K$ -band flux companion, but such an object would then be the primary component of the system and therefore dominate the overall SED. This possibility is excluded by the clear late-T spectral type in the  $Y$ ,  $J$ , and  $H$  bands, as well as with the strong  $\text{CH}_4$  absorption band at  $2.2 \mu\text{m}$ . There are other unlikely but still plausible binary

scenarios that could account for part of the spectral peculiarity of CFBDSIR 2149, such as a partially obscured late-L or early-T companion or even a Y dwarf companion with atypically strong  $K$ -band flux. The fact that CFBDSIR 2149 is significantly brighter than GJ 758B may favour a hypothesis that CFBDSIR 2149 is an unresolved equal-mass binary, but then the components would be nearly equal in flux at all wavelengths and thus not explain the atypical shape of their individual SEDs. Finally we point out that the existence of any lower-mass, cooler companion would be most visible in the thermal infrared, however, as can be seen in the lower right panel of Fig. 1, the IRAC absolute photometry of CFBDSIR 2149 is exactly what is expected for a single late T dwarf. This makes the binarity scenario highly implausible.

### 5.5. CFBDSIR 2149 as an unusually dusty brown dwarf

Dust enhancement has long been used to explain atypically red colours in L and early-T dwarfs, and dust reddening could account for some of the trends observed in the difference between the best fit and observed spectra (see Fig. 4). Without dust, the models used here have a flux excess in the bluer part of the spectrum and a flux deficit in the redder parts compared to CFBDSIR 2149. The work of Marocco et al. (2014) shows that atypically red L dwarfs can be remarkably well fitted to typical L dwarf templates of the same spectral type after a simple dereddening by iron-corundum dust. This hypothesis could explain the very red  $J - K$  colour and does provide quite good fit to the overall spectrum of CFBDSIR 2149 (F. Marocco, priv. comm.), but it does not fully account for its blue  $J - H$  colour. Indeed, reddening by dust is correlated with wavelength and should therefore also cause a reddening of the  $H$  band. Another issue is that it seems difficult to explain how dust could be maintained above the photosphere of such a cold late-T atmosphere without settling. The dust hypothesis also struggles to account for the weak KI doublet observed in the spectra of CFBDSIR 2149 (Table 4) because enhanced dust abundance would not affect such narrow spectral features despite its potentially strong impact on the overall SED. Finally we note that the best fits with the Ma&Mo2017 model grid, which include a parameter for the condensation speed of dust always converge toward either the fastest dust condensation speed, leading to very few dust in the photosphere, or to the *no cloud* setting, which explicitly removes all dust from the atmosphere. This is strongly at odds with the hypothesis that CFBDSIR 2149 is an unusually dusty brown dwarf.

## 6. Conclusions

We conducted a multi-instrument, multi-wavelength follow-up of CFBDSIR 2149 and determined its parallax (corresponding to a distance of  $54.6 \pm 5.4$  pc), as well as its six-dimensional position and kinematics. These results show that it is very unlikely that CFBDSIR 2149 is a member of the AB Doradus moving group, as claimed by Delorme et al. (2012), therefore removing any strong independent constraint on its age. We also obtained deep NIR spectroscopic observations as well as *Spitzer* photometry in the mid-infrared. Together with the knowledge of its distance, this allowed us to carry out an in-depth spectral analysis of CFBDSIR 2149, notably using absolute and bolometric fluxes, confirming its peculiar nature. Our conclusions are that CFBDSIR 2149 is most probably either a young ( $< 500$  Myr) isolated planetary-mass ( $2-13 M_{\text{Jup}}$ ) object of late-T spectral type, or an older ( $2-3$  Gyr), metallicity-enhanced,  $2-40 M_{\text{Jup}}$  brown dwarf. Our theoretical understanding of cool,

low-gravity and/or metallicity-enhanced atmospheres is not yet robust enough to decisively discriminate between these two hypotheses, especially because these physical parameters have very similar effects on the emergent spectra of such atmospheres. However, we point out that there is a distinctive impact on the *J*-band KI doublet, that does not appear to be significantly affected by low gravity at constant effective temperature, while high metallicity strongly increases its equivalent width. Thus, the KI doublet could be a crucial tool for discriminating between low-gravity planetary-mass objects and high-metallicity brown dwarfs. In the case of CFBDSIR 2149, the relatively weak KI doublet favours the hypothesis that it is a young, low-gravity planetary mass object. Good low to intermediate gravity fits to the data can be obtained with BT-settl models for both solar and  $[M/H] = 0.3$  metallicity and for solar metallicity only with Ma&Mo2017 models. If CFBDSIR 2149 is a higher gravity, higher mass brown dwarf then our data are only consistent with models at super-solar metallicity, which is a relatively rare occurrence in the solar neighbourhood. Finally, we point out that CFBDSIR 2149 may be similar in spectral properties, and perhaps also in mass and age, to the recently discovered exoplanet 51 Eri b (Macintosh et al. 2015).

*Acknowledgements.* We thank the anonymous referee for his/her valuable comments. This work is based on observations obtained with MegaPrime/MegaCam, a joint project of CFHT and CEA/DAPNIA, at the Canada-France-Hawaii Telescope (CFHT) which is operated by the National Research Council (NRC) of Canada, the Institut National des Sciences de l'Univers of the Centre National de la Recherche Scientifique (CNRS) of France, and the University of Hawaii. This work is based in part on data products produced at TERAPIX and the Canadian Astronomy Data Centre as part of the Canada-France-Hawaii Telescope Legacy Survey, a collaborative project of NRC and CNRS. "This research has made use of the NASA/IPAC Infrared Science Archive, which is operated by the Jet Propulsion Laboratory, California Institute of Technology, under contract with the National Aeronautics and Space Administration". We acknowledge financial support from "Programme National de Physique Stellaire" (PNPS) of CNRS/INSU, France. We acknowledge financial support from the French ANR GIPSE, ANR-14-CE33-0018. DH is supported by the Collaborative Research Centre SFB 881 "The Milky Way System" (subproject A4) of the German Research Foundation (DFG).

## References

- Ahn, C. P., Alexandroff, R., Allende Prieto, C., et al. 2012, *ApJS*, 203, 21
- Allard, F. 2014, in IAU Symp. 299, eds. M. Booth, B. C. Matthews, & J. R. Graham, 271
- Allard, N. F., Allard, F., & Kielkopf, J. F. 2005, *A&A*, 440, 1195
- Allard, F., Homeier, D., & Freytag, B. 2012, *Roy. Soc. London Phil. Trans. Ser. A*, 370, 2765
- Baraffe, I., Chabrier, G., Barman, T. S., Allard, F., & Hauschildt, P. H. 2003, *A&A*, 402, 701
- Bardalez Gagliuffi, D. C., Burgasser, A. J., Gelino, C. R., et al. 2014, *ApJ*, 794, 143
- Bell, C. P. M., Mamajek, E. E., & Naylor, T. 2015, *MNRAS*, 454, 593
- Bertin, E., & Arnouts, S. 1996, *A&AS*, 117, 393
- Bonnefoy, M., Zurlo, A., Baudino, J. L., et al. 2016, *A&A*, 587, A58
- Boone, R. H., King, J. R., & Soderblom, D. R. 2006, *New Astron. Rev.*, 50, 526
- Burgasser, A. J., Kirkpatrick, J. D., Cutri, R. M., et al. 2000, *ApJ*, 531, L57
- Burgasser, A. J., Kirkpatrick, J. D., Lepine, S., et al. 2004, *BAAS*, 36, 1352
- Burgasser, A. J., Geballe, T. R., Leggett, S. K., Kirkpatrick, J. D., & Golimowski, D. A. 2006, *ApJ*, 637, 1067
- Burningham, B., Pinfield, D. J., Leggett, S. K., et al. 2009, *MNRAS*, 395, 1237
- Burningham, B., Leggett, S. K., Lucas, P. W., et al. 2010, *MNRAS*, 404, 1952
- Burningham, B., Leggett, S. K., Homeier, D., et al. 2011, *MNRAS*, 414, 3590
- Burrows, A., Marley, M., Hubbard, W. B., et al. 1997, *ApJ*, 491, 856
- Burrows, A., Sudarsky, D., Lunine, J. I., et al. 2003, *ApJ*, 596, 587
- Canty, J. I., Lucas, P. W., Yurchenko, S. N., et al. 2015, *MNRAS*, 450, 454
- Casali, M., Pirard, J.-F., Kissler-Patig, M., et al. 2006, in *SPIE Conf. Ser.*, 6269, 62690W
- Chauvin, G., Lagrange, A.-M., Zuckerman, B., et al. 2005, *A&A*, 438, L29
- Delorme, P., Delfosse, X., Albert, L., et al. 2008a, *A&A*, 482, 961
- Delorme, P., Willott, C. J., Forveille, T., et al. 2008b, *A&A*, 484, 469
- Delorme, P., Gagné, J., Malo, L., et al. 2012, *A&A*, 548, A26
- Delorme, P., Gagné, J., Girard, J. H., et al. 2013, *A&A*, 553, L5
- Devillard, N. 2001, in *Astronomical Data Analysis Software and Systems X*, eds. F. R. Harnden, Jr., F. A. Primini, & H. E. Payne, *ASP Conf. Ser.*, 238, 525
- Dupuy, T. J., & Kraus, A. L. 2013, *Science*, 341, 1492
- Dupuy, T. J., & Liu, M. C. 2012, *ApJS*, 201, 19
- Faherty, J. K., Rice, E. L., Cruz, K. L., Mamajek, E. E., & Núñez, A. 2013, *AJ*, 145, 2
- Faherty, J. K., Beletsky, Y., Burgasser, A. J., et al. 2014, *ApJ*, 790, 90
- Fazio, G. G., Hora, J. L., Allen, L. E., et al. 2004, *ApJS*, 154, 10
- Gagné, J., Lafrenière, D., Doyon, R., Malo, L., & Artigau, É. 2014, *ApJ*, 783, 121
- Gagné, J., Burgasser, A. J., Faherty, J. K., et al. 2015, *ApJ*, 808, L20
- Gauza, B., Béjar, V. J. S., Pérez-Garrido, A., et al. 2015, *ApJ*, 804, 96
- Gizis, J. E., Allers, K. N., Liu, M. C., et al. 2015, *ApJ*, 799, 203
- Golimowski, D. A., Leggett, S. K., Marley, M. S., et al. 2004, *AJ*, 127, 3516
- Hiranaka, K., Cruz, K., & Marley, M. 2012, in *AAS Meeting Abstracts*, 219, 345.29
- Hiranaka, K., Cruz, K. L., Douglas, S. T., Marley, M. S., & Baldassare, V. F. 2016, *ApJ*, 830, 96
- Johnson, D. R. H., & Soderblom, D. R. 1987, *AJ*, 93, 864
- Kellogg, K., Metchev, S., Gagné, J., & Faherty, J. 2016, *ApJ*, 821, L15
- Kirkpatrick, J. D., Gelino, C. R., Cushing, M. C., et al. 2012, *ApJ*, 753, 156
- Kissler-Patig, M., Pirard, J.-F., Casali, M., et al. 2008, *A&A*, 491, 941
- Knapp, G. R., Leggett, S. K., Fan, X., et al. 2004, *AJ*, 127, 3553
- Kumar, S. S. 1963, *ApJ*, 137, 1121
- Kuzuhara, M., Tamura, M., Kudo, T., et al. 2013, *ApJ*, 774, 11
- Leggett, S. K., Hauschildt, P. H., Allard, F., Geballe, T. R., & Baron, E. 2002, *MNRAS*, 332, 78
- Liu, M. C., Magnier, E. A., Deacon, N. R., et al. 2013, *ApJ*, 777, L20
- Lodders, K., & Fegley, Jr., B. 2006, in *Astrophysics Update 2*, ed. J. W. Mason, 1
- Luhman, K. L. 2014, *ApJ*, 786, L18
- Macintosh, B., Graham, J. R., Barman, T., et al. 2015, *Science*, 350, 64
- Makovoz, D., & Marleau, F. R. 2005, *PASP*, 117, 1113
- Malo, L., Doyon, R., Lafrenière, D., et al. 2013, *ApJ*, 762, 88
- Marocco, F., Day-Jones, A. C., Lucas, P. W., et al. 2014, *MNRAS*, 439, 372
- Marois, C., Macintosh, B., & Véran, J.-P. 2010, in *SPIE Conf. Ser.*, 7736, 77361
- McLean, I. S., McGovern, M. R., Burgasser, A. J., et al. 2003, *ApJ*, 596, 561
- McLean, I. S., Prato, L., McGovern, M. R., et al. 2007, *ApJ*, 658, 1217
- Modigliani, A., Goldoni, P., Royer, F., et al. 2010, in *SPIE Conf. Ser.*, 7737, 773728
- Morley, C. V., Fortney, J. J., Marley, M. S., et al. 2012, *ApJ*, 756, 172
- Morley, C. V., Marley, M. S., Fortney, J. J., et al. 2014, *ApJ*, 787, 78
- Nidever, D. L., Marcy, G. W., Butler, R. P., Fischer, D. A., & Vogt, S. S. 2002, *ApJS*, 141, 503
- Peña Ramírez, K., Béjar, V. J. S., Zapatero Osorio, M. R., Petr-Gotzens, M. G., & Martín, E. L. 2012, *ApJ*, 754, 30
- Pirard, J.-F., Kissler-Patig, M., Moorwood, A., et al. 2004, in *Ground-based Instrumentation for Astronomy*, eds. A. F. M. Moorwood, & M. Iye, *SPIE Conf. Ser.*, 5492, 1763
- Puget, P., Stadler, E., Doyon, R., et al. 2004, in *SPIE Conf. Ser.* 5492, eds. A. F. M. Moorwood, & M. Iye, 978
- Radigan, J. 2014, *ApJ*, 797, 120
- Robin, A. C., Reylé, C., Derrière, S., & Picaud, S. 2003, *A&A*, 409, 523
- Samland, M., Mollière, P., Bonnefoy, M., et al. 2017, *A&A*, in press DOI: 10.1051/0004-6361/201629767
- Schlegel, D. J., Finkbeiner, D. P., & Davis, M. 1998, *ApJ*, 500, 525
- Schneider, A. C., Cushing, M. C., Kirkpatrick, J. D., et al. 2014, *AJ*, 147, 34
- Schneider, A. C., Windsor, J., Cushing, M. C., Kirkpatrick, J. D., & Wright, E. L. 2016, *ApJ*, 822, L1
- Skemer, A. J., Close, L. M., Szűcs, L., et al. 2011, *ApJ*, 732, 107
- Skemer, A. J., Morley, C. V., Zimmerman, N. T., et al. 2016, *ApJ*, 817, 166
- Skrutskie, M. F., Cutri, R. M., Stiening, R., et al. 2006, *AJ*, 131, 1163
- Thalmann, C., Carson, J., Janson, M., et al. 2009, *ApJ*, 707, L123
- Tremblin, P., Amundsen, D. S., Mourier, P., et al. 2015, *ApJ*, 804, L17
- Vernet, J., Dekker, H., D'Odorico, S., et al. 2011, *A&A*, 536, A105
- Vigan, A., Bonnefoy, M., Ginski, C., et al. 2016, *A&A*, 587, A55
- Visscher, C., Lodders, K., & Fegley, Jr., B. 2010, *ApJ*, 716, 1060
- Warren, S. J., Mortlock, D. J., Leggett, S. K., et al. 2007, *MNRAS*, 381, 1400
- Yurchenko, S. N., & Tennyson, J. 2014, *MNRAS*, 440, 1649
- Zapatero Osorio, M. R., Béjar, V. J. S., Martín, E. L., et al. 2002, *ApJ*, 578, 536
- Zapatero Osorio, M. R., Gálvez Ortiz, M. C., Bihain, G., et al. 2014, *A&A*, 568, A77